Solid State Spectroscopy II
— XAFS, PES —

(BL1A, 4B, 5A, 7A, 8B1, 8B2)

(BL-1A)

Al K XANES analysis of the local structure around Al in Al-EDTA-F complex

Hisao YAMASHIGE[1*], Yuichi TATEISHI[1], Tsutomu KURISAKI[1], Hisanobu WAKITA[1, 2]

[1]*Department of Chemistry, Faculty of Science, Fukuoka University, Nanakuma, Jonan-ku, Fukuoka 814-0180, Japan*

[2]*Advanced Materials Institute, Fukuoka University, Nanakuma, Jonan-ku, Fukuoka 814-0180, Japan*

*Corresponding author: sd022501@cis.fukuoka-u.ac.jp

Though hydrated Al ion has strong toxicity in soil, its toxicity decreases by the complex formation with natural organic compounds which mainly possesses carboxyl group. Therefore, it is important for environmental sciences to clarify the interaction between Al and natural organic compounds under the molecular level [1]. It is essential to investigate the interaction between Al ions and simple model compounds. So, we employed EDTA (ethylenediaminetetraacetate) as a model compound of natural organic compounds.

The X-ray absorption spectra were measured at BL-1A of the UVSOR in the Institute of Molecular Science, Okazaki [2]. The Al K-edge XANES spectra for the Al-EDTA-Na complex and Al-EDTA-K complex with pH4.5 and 6 are shown in Figs. 1 and 2. A change in the spectral patterns was observed depending on the Na ion and K ion. For each pH the difference of the peak intensity was also observed between Al-EDTA-Na and Al-EDTA-K complex, respectively. We are going to try to analyze these changes from a comparison of Al K-edge XANES and the calculated spectra by molecular orbital calculations.

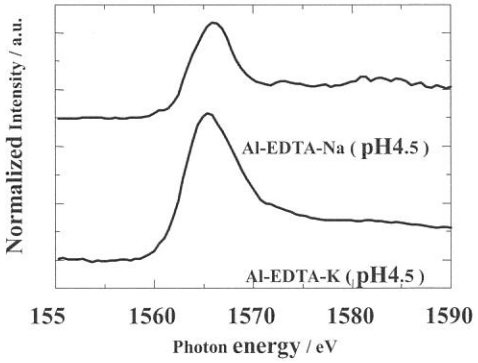

Fig. 1. Al K-edge XANES spectra of Al-EDTA complexes (pH4.5).

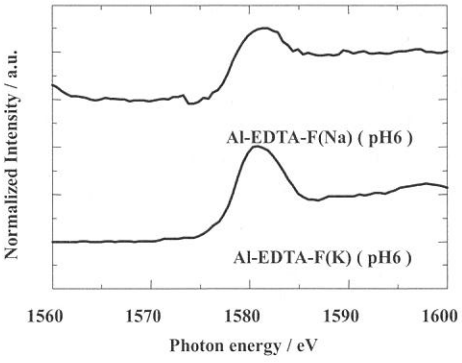

Fig. 2. Al K-edge XANES spectra of Al-EDTA complexes (pH6.0).

References

[1] S. Matsuo, H. Wakita, *Structural Chemistry*, **14**, 69 (2003)

[2] S. Murata, T. Matsukawa, S. Naoè, T. Horigome, O. Matsuodo, and M. Watanabe, *Rev. Sci. Instrum.*, **63**, 1309 (1992)

(BL1A)(BL8B1)

Electronic structure change in $LiNi_{0.5}Mn_{0.5}O_2$ cathode materials for Lithium-ion secondary batteries from transition metal *L*-edge and oxygen *K*-edge spectroscopy

Yoshinori ARACHI, Takeshi ASAI

Faculty of Engineering, Kansai University, Osaka 564-8680, Japan

Hironori KOBAYASHI

†*National Institute of Advanced Industrial Science and Technology(AIST),Osaka 563-8577*

Shuichi EMURA

††*ISIR, Osaka University, Ibaraki, Osaka 567-0047*

In view of small natural deposits of Co and its toxicity, new cathode materials that can serve as alternatives to $LiCoO_2$ in lithium ion batteries have been extensively pursued. Several problems including thermal stability and capacity fading at elevated temperatures limit practical utilization and few materials satisfy all properties that support high performance. Recently, $LiNi_{0.5}Mn_{0.5}O_2$ has been proposed as a new cathode material for rechargeable lithium batteries.[1] Cell performance using Li exhibited good cycleability, and a reversible capacity of 150 mAh / g within the voltage range of 3.0 to 4.3 V, which corresponds to one-half of theoretical capacity (280mAh/g). Synchrotron X-ray diffraction and XAFS measurement have been employed to investigate structural change and the charging process of a layered-$LiNi_{0.5}Mn_{0.5}O_2$ cathode material (Fig.1). The structure of charged $Li_{1-x}Ni_{0.5}Mn_{0.5}O_2$ (x=0.5), which corresponds to the composition for showing rechargeable capacity, was determined. In this study, the electronic structural change due to charging process was investigated by XANES spectra of Ni, Mn *K*- and *L*-edges, and O *K*-edge.

Samples were prepared from $LiOH{\cdot}H_2O$ and dry precipitates of $Ni(OH)_2$ and $Mn(OH)_2$. They were mixed and then calcinated at 873K for 12 h. The obtained powders were pressed into a disk under a pressure of 5 t/cm^2, and sintered at 1273K for 12 h. Lithium was electrochemically deintercalated at a rate of 170 μA / cm^2, by use of a coin-type cell. The cathode material was composed of the following materials; sample: acetylene black: poly vinylidene fluoride (PVdF)=86:4:10 in wt%, and 1M $LiClO_4$ in propylene carbonate(PC):1,2-dimethoxycarbonate(DMC)=1:1 by volume was used as the electrolyte. Rietveld crystal structural refinement was carried out by use of the program RIETAN-2000. X-ray absorption measurements at the Mn and Ni *L*-edges, and O *K*-edge by total electron yield and fluorescence yield were performed on BL1A and BL8B1.

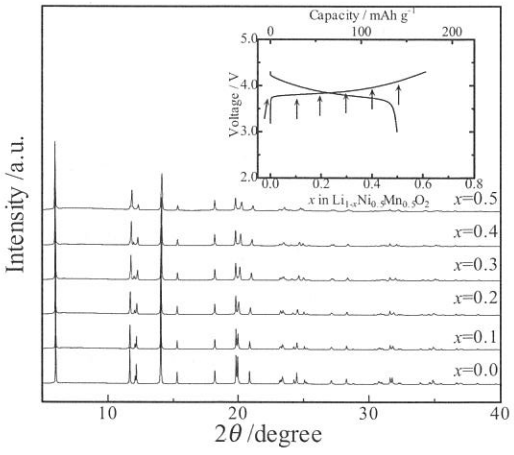

Fig.1. X-ray diffraction patterns for $Li_{1-x}Ni_{0.5}Mn_{0.5}O_2$. Lithium was electrochemically deintercalated at a rate of 170μA/cm^{2}using coin-type cell. The insert shows Charge and Discharge curves of the Li/$Li_{1-x}Ni_{0.5}Mn_{0.5}O_2$ cell measured with a current density of 0.1mA/cm^2 and cut-off voltages of 3.0 and 4.3 V.

Fig.1 shows the XRD patterns for lithium-deintercalated samples. Each sample corresponds to the composition in the charge curve. The ion distribution indicated that a small amount of Ni (occupancy, g=0.093) occupies the Li (3b)site.[2,3] The lattice parameters changed in accordance with decreased ionic radius of oxidized transition metals and electrostatic repulsive force between oxygen ions in association with the phase transition from hexagonal (*R3m*) to monoclinic (*C2/m*) resulting from the ordering of cations in the layered structure, after lithium is extracted. Fig.2 shows the XANES spectra of Ni L-edge for charged $Li_{1-x}Ni_{0.5}Mn_{0.5}O_2$. The sample of x=0.7 and x=0.8 were prepared by different electrochemical condition from that of Fig.1. The peaks corresponding to L_{III}, L_{II} showed a chemical shift towards higher energy within the voltage range of 3.0-4.1V.

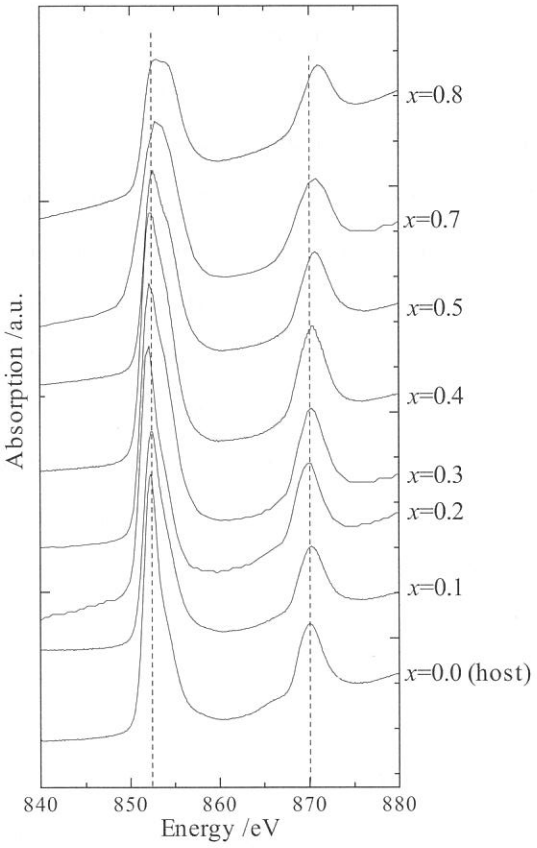

Fig.2 Ni L-edge XANES of $Li_{1-x}Ni_{0.5}Mn_{0.5}O_2$.

On the other hand, that of Mn L-edge showed no chemical shifts. For the host material (x=0.0), Ni and Mn were in divalent and tetravalent valence state by comparing spectra with NiO, $LiNiO_2$ and Li_2MnO_3. Thus, the charging process of this material up to x=0.5 was proceeded by continuous oxidation of Ni, not oxidation of Mn. XAFS of Ni K-edge and Mn support these results well. Fig.3 shows the XANES spectra of O K-edge which were obtained by fluorescence yield (F.Y.) for charged $Li_{1-x}Ni_{0.5}Mn_{0.5}O_2$. In F.Y. mode the sampling depth is much deeper than in the electron yield. These spectra reflect on the internal chemical state of the sample. The broad peak about 547-552eV may correspond to the transition to the band composed with metal(Ni,Mn)3d and O2p. The explanation of O K-edge spectra in details using first principle calculation are under progress.

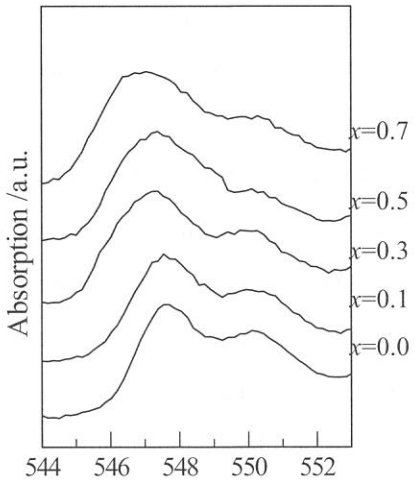

Fig.3 O K-edge XANES of $Li_{1-x}Ni_{0.5}Mn_{0.5}O_2$.

References

1. T.Ohzuku and Y.Makimura, *Chem.Lett.*, (2001)744.
2. Y.Arachi, et al, *Chem.Lett.*, (2003)60.
3. H.Kobayashi et al, *J.Materials Chem.*, **13**(2003)590.

(BL1A)

Mo L_{III}-edge XANES Study of Catalytically Active Molybdenum Species on Zeolite Supports for Dehydroaromatization of Lower Alkanes

Hirofumi Aritani,* Masato Tamai,** Fumihide Nishimura,** Shinji Konishi,**
Chikako Karatani,** Takayuki Murakami** and Atsushi Nakahira**

**Faculty of Engineering, Saitama Institute of Technology, Okabe, Saitama 369-0293, Japan.*;

***Faculty of Engineering & Design, Kyoto Institute of Technology, Sakyo-ku, Kyoto 606-8585, Japan.*

MoO_3-modified H-ZSM-5 zeolite (Mo/H-ZSM5) catalysts are noted for high and selective activity of dehydroaromatization; it is a novel and valuable catalysis because of producing petrochemical products from natural gas directly. During the conversion of methane or ethane to benzene, supported molybdenum ions (Mo^{6+}) are almost reduced to low-valence ions, Mo^{2+} (in Mo_2C, as a suggested species) or others. At the same time, coke deposition on the catalyst surface proceeds. Reactivity of dehydroaromatization strongly relates to both reduction of Mo ions and coke deposition, and the relation is important to solve the reaction mechanism of dehydroaromatization catalysis. In addition, reaction pathways to form benzene are also important. But details of them have been unclear. In particular, important insights about the local structure of active Mo species and its formation on zeolite support in the reaction are still unknown. We have studied the catalytic activity of dehydroaromatization of methane or ethane on Mo-modified H-ZSM5 zeolite catalysts. It is summarized that MoO_3/HZSM-5 and MoO_3/H-BEA (Beta-zeolite) show selective activity for dehydroaromatization of methane. In these cases, 7.5wt% of MoO_3-loading amount shows the maximum yield of benzene. On the other hand, MoO_3/SiO_2-Al_2O_3 (amorphous silica-alumina) shows quite high activity for dehydroaromatization of ethane, although it shows low activity for dehydroaromatization of methane. As described above results, property of silica-alumina support affects the molybdenum species as catalytically active sites. Thus we characterized the active Mo spices on silica-alumina (amorphous silica-alumina and several types of zeolites) supports by means of Mo L_{III}-edge XANES. In this report, local structure of supported Mo ions and their redox changes after dehydroaromatization of methane or ethane at 973 K for 3 h.

All the catalyst samples were prepared by impregnation of each silica-alumina support with AHM ($(NH_4)_6Mo_7O_{24}\cdot 4H_2O$) solution, and followed by drying and calcination at 773 K for 3 h. Amount of MoO_3-loading is 7.5wt% in all the samples. Amorphous SiO_2-Al_2O_3 (JRC-SAH-1, 28.6wt%-Al_2O_3), H-ZSM5 (JRC-Z5-90H, Si/Al_2=90), and H-BEA (JRC-H-BEA25, Si/Al_2=25) were employed as catalyst supports. Mo L_{III}-edge XANES spectra were measured in BL1A of UVSOR-IMS in total-electron yield (TEY) mode.

Figure 1 shows the L_{III}-edge XANES of authentic Mo compounds with several atomic valences. It is clear that edge energy values of XANES in Mo_2C (Mo^{2+}) and Mo metal are lower than those of Mo^{6+} compounds (AHM and MoO_3). However, difference between Mo_2C and Mo metal (maybe oxidized in air) cannot be seen in

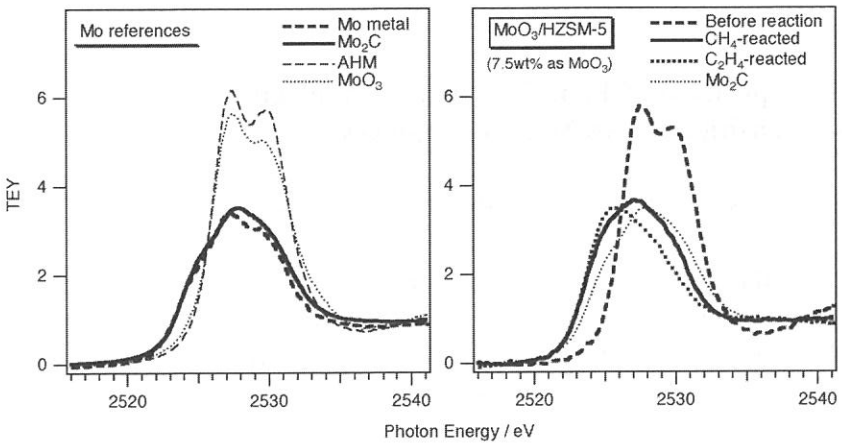

Figire 1 Mo L_{III}-edge XANES spectra of MoO_3(7.5wt%)/H-ZSM5 before/after the reaction with methane or ethane (right). The spectra of authentic Mo compounds are also shown (left).

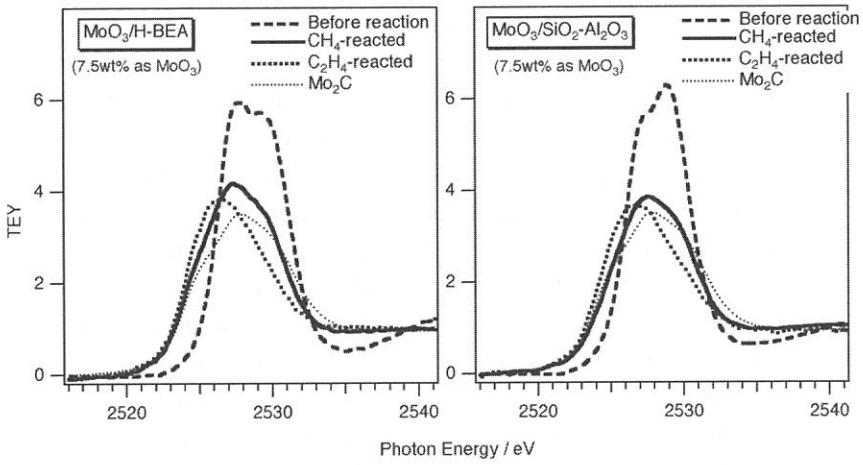

Figire 2 Mo L_{III}-edge XANES spectra of MoO_3(7.5wt%)/H-BEA (left) and MoO_3/SiO_2-Al_2O_3 (right) before/after the reaction with methane or ethane.

this result. In case of MoO_3/H-ZSM5 shown in Figure 1, the spectrum indicates the presence of distorted octahedra of Mo^{6+} species before the reaction. After the reaction with methane, change of the XANES spectrum due to reduction of Mo ions is definitely. The edge energy is lower than that of Mo_2C, suggesting the reduced site with Mo metal species. After the reaction with ethane, the similar change of XANES spectrum can also be seen. These results indicate the formation of metallic Mo species on H-ZSM5 support by the reaction with lower alkanes. Figure 2 shows the XANES spectra of MoO_3/H-BEA and MoO_3/SiO_2-Al_2O_3 (amorphous silica-alumina) before/after the dehydroaromatization. In case of MoO_3/H-BEA, the spectral feature of XANES before/after the reaction is almost similar to those of MoO_3/H-ZSM5, however, the edge energy after the reaction (with methane and ethane) is slightly higher than those of MoO_3/H-ZSM5. Thus it is concluded that H-ZSM5 support affects the acceleration of Mo reduction in contact with alkanes during the dehydroaromatization. It suggests the difference of dehydroaromatization activity between H-ZSM5 and H-BEA supports. For MoO_3/SiO_2-Al_2O_3, Mo^{6+} tetrahedra are dominated before the reaction, which is different form those on zeolite (H-ZSM5 and H-BEA) supports. After the reaction, XANES spectra also suggest the reduction of Mo ions. However, the reduction degree is the least for supported catalysts, and formation of Mo_2C-like species is suggested. Thus amorphous SiO_2-Al_2O_3 gives low effect for reduction of mo ions during the reaction. In this case, high activity for ethane dehydroaromatization is obtained. It is concluded that catalytic activity for dehydroaromatization relates to the reduced state of Mo ions. It suggests that metallic Mo needs to activate methane, and Mo_2C-like species (with lower reduced ion) is available for ethane dehydroaromatization.

(BL1A)

X-Ray Absorption Spectra on Cl and Br Ligands Involved with First Transition Series Metal Complexes

Shuji MATSUO[1*], Tsutomu KURISAKI[2], Hisao YAMASHIGE[2], and Hisanobu WAKITA[1,2]

[1]*Advanced Materials Institute, Fukuoka University, Nanakuma, Jonan-ku, Fukuoka 814-0180, Japan*
[2]*Department of Chemistry, Faculty of Science, Fukuoka University, Nanakuma, Jonan-ku, Fukuoka 814-0180, Japan*

*Corresponding author: mashu23@hotmail.com

Characterization of metal complexes using x-ray absorption spectroscopy has been made extensively for metal atom. Recently, with becoming popular to use soft x-ray beam at synchrotron radiation facilities, the absorption edges of atoms coordinated to the center metal have been also measured to obtain more detail information on ligand-metal bonding interaction and electron state because the spectra show better resolved features corresponding to the electron state of valence and conduction bands due to long core-hole lifetime [1]. So far, we synthesized [$CuBr_2$(cyclam)] (cyclam = 1,4,8,11-tetraazacyclotetradecane) and measured the x-ray absorption near-edge structure (XANES) spectra near the Cu K-edge of the complex in crystal and in water [2]. As a result, we found that the XANES spectrum for the crystalline sample was different from that for the solution sample, and that from single structure analysis, there were two Br atoms on the axial position to Cu atom with 2.96 Å away. We have thus concluded that the crystalline and solution structures of [$CuBr_2$(cyclam)] differ in the coordination at the axial sites to Cu atom. Furthermore, this result suggests another aspect that ligands can serve as probe to investigate the chemical states of center metal atom in a complex from XANES of the ligands [3]. In this study, we measured the XANES spectra for Cl and Br atoms as a ligand in several first transition series metal complexes to examine the relations between a ligand and a center metal atom, and between a ligand and another one via a center metal atom.

The x-ray absorption spectra were measured at BL1A, which is equipped with a focusing premirror and a double crystal monochromator [4], of the UVSOR in the Institute of Molecular Science, Okazaki, Japan. The ring energy of the UVSOR storage ring was 750 MeV and the stored current was 110–230 mA. The x-ray absorption spectra near the Cl K- and Br $L_{2,3}$-edges were recorded in the regions of 2800-3000 eV by use of two Ge(111) crystals and of 1500-1700 eV by use of two KTP(011) crystals, respectively. The absorption was monitored by the total electron yield using a photomultiplier. The measured samples were [$CoCl_2$(cyclam)]PF_6, [MCl_2(cyclam)] (M = Ni, Cu, and Zn), [MBr_2(cyclam)] (M = Ni, and Cu), [$Cu(en)_2$]Br_2 (en = ethylenediamine), and [$CuBr_2(en)(H_2O)_2$]. All powder samples were spread on carbon adhesive sheets to be adhered to the first dynode of the photomultiplier.

The Cl K-edge XANES spectra for [$CoCl_2$(cyclam)]PF_6 and [MCl_2(cyclam)] (M = Ni, Cu, and Zn) are shown in Fig. 1. The features of the spectra indicate to change by d^n configuration of the transition metal ion. Of course, the effects of spin state, metal-ligand bond length, and the split of d orbitals due to geometry in connection with the changes must be considered when we discuss the features of the spectra [5]. Second derivatives of the original data in Fig. 1 are shown in Fig. 2 with arrows on meaningful features corresponding to the XANES spectra in Fig. 1. The main absorption in the region of 2825 - 2827 eV in Fig. 1 originates from a Cl 1s → 4p transition. Since Co, Ni, and Cu ions are d-opened-shell ions, the pre-edge peak and/or shoulder on the main edge rise on each spectrum in Fig. 1, which can be seen as peaks in Fig. 2, result from the transition from a Cl 1s orbital to the molecular orbitals of the metal 3d and Cl 3p orbitals [3,5]. However, we presume that the shoulders on the main edge rise may be caused by the transition to the molecular orbitals of the metal 3d and Cl 4p orbitals because they neighbor the peak of the Cl 1s → 4p transition. On the other hand, in the case of the Zn complex with a d-closed-shell ion, only one peak due to

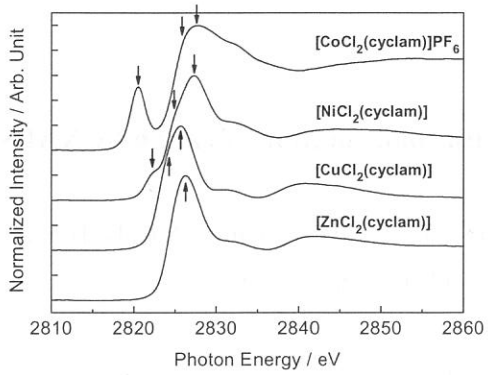

Fig. 1 Normalized Cl K-edge XANES spectra of Cl ion as a ligand to the metal-cyclam complexes.

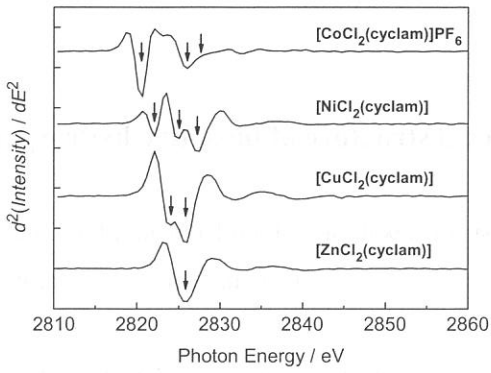

Fig. 2 Second derivatives of the spectra in Fig. 1.

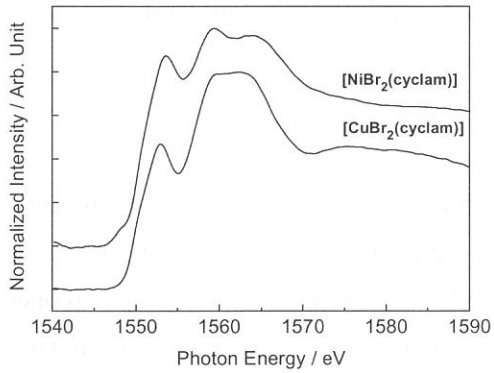

Fig. 3 Normalized Br L_3-edge XANES spectra of Br ion as a ligand to the Ni- and Cu-cyclam complexes.

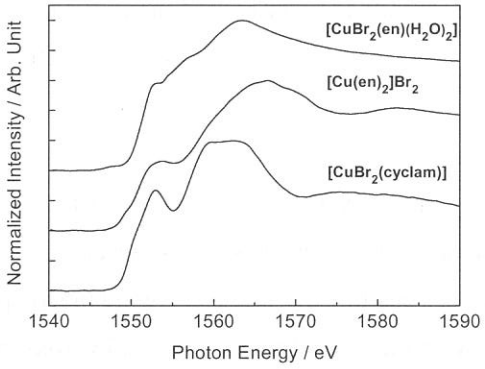

Fig. 4 Normalized Br L_3-edge XANES spectra of Br ion as a ligand to Cu-cyclam and -en complexes.

the Cl 1s → 4p transition can be seen on the spectrum.

The XANES spectra near the Br L_3-edge for $[CuBr_2(cyclam)]$ and $[NiBr_2(cyclam)]$, and for $[CuBr_2(cyclam)]$ $[Cu(en)_2]Br_2$, and $[CuBr_2(en)(H_2O)_2]$ are shown in Figs. 3 and 4, respectively. We presume that each peak between 1550 and 1570 eV may results from a Br $2p_{3/2}$ → 4d transition. In this case, the 4d manifold is probably split by bonding interaction between center metal and Br orbitals, however, the energy levels of d orbitals in this case may be different from those of octahedral geometry. In Fig. 3, each peak position of $[CuBr_2(cyclam)]$ is slightly different from corresponding each peak position of $[NiBr_2(cyclam)]$. This is likely to be due to the difference between Cu–Br and Ni-Br bonding interactions. When ethylendiamine replaced cyclam, the split of Br 4d manihold is expected to change by the change of Cu-Br bonding interaction in connection with coordination geometry. This suggestion could be considered to be reasonable by the result that the features of three spectra in Fig. 4 are remarkably different among them. However, the assignments of the peaks on Br L_3-edge XANES spectra is unsatisfactorily discussed because there are a few reports on the Br L_3-edge XANES measurements, especially for Br ion such as ligand to metal complex. Detailed interpretation using discrete variational Xα molecular-orbital calculations is in progress.

This study is supported by the Advanced Materials Institute of Fukuoka University.

References

[1] H. Wakita, *Bunseki*, **2002**, 24.

[2] S. Matsuo, T. Yamaguchi, and H. Wakita, *Adv. Quantum Chem.*, **37**, 153 (2000).

[3] A. Rompel, J. C. Andrews, R. M. Cinco, M. W. Wemple, G. Christou, N. A. Law, V. L. Pecoraro, K. Sauer, V. K. Yachandra, and M. P. Klein, *J. Am. Chem. Soc.*, **119**, 4465 (1997).

[4] A. Hiraya, T. Horigome, N. Okada, N. Mizutani, K. Sakai, O. Matsudo, M. Hasumoto, K. Fukui, and M. Watanabe, *Rev. Sci. Instrum.*, **63**, 1264 (1992).

[5] B. Hedman, K. O. Hodgson, and E. I. Solomon, *J. Am. Chem. Soc.*, **112**, 1643 (1990); T. Glaser, B. Hedman, K. O. Hodgson, and E. I. Solomon, *Acc. Chem. Res.*, **33**, 859 (2000).

(BL1A)

Local structure of bioactive hydroxyapatite with solid solution of cation by XAFS

Atsushi Nakahira*, Shinji Konishi*, Fumihide Nishimura*, Takayuki Murakami*, Yukako Honda*, Chikako Karatan*, Masato.Tamai*, and Hirofumi. Aritani**

* Dept. of Chem. and Mater., Faculty of Engineering and Design., Kyoto Institute of Technology, Matsugasaki Sakyou, Kyoto 606-8585, Japan

** Department of Chemistry, Faculty of Engineering, Saitama Institute of Technology, Okabe-cho, Saitama 369-0293, Japan

Hydroxyapatite, $Ca_{10}(PO_4)_6(OH)_2$, is one of most attractive bioceramics for implants and replacements in orthopedics fields, because it is similar to the inorganic components of bone and teeth and at the same time possesses the good biocompatibility and the excellent biologically active properties. Actually, in the case of implanting the hydroxyapatite bodies in the human body, the fast precipitation of bone-like hydroxyapatite crystal on the surface of the implant are needed. It is well known that natural bone have more excellent biocompatibility and osteoconductive, since these bones contain generally some cations in the hydroxyapatite, such as Fe, Mg and Zn etc. Nevertheless, it is thought that the local structures around P and Ca in hydroxyapatite with cation are related to their biocompatibility and osteoconduction. Therefore, the investigation about the effect of the cation on fine structure in hydroxyapatite is important for high performance bioceramics.

Highly pure hydroxyapatite powders (HAP200) were used. This hydroxyapatite had rod-like morphology with the average particle size of some hundreds nm. The powder was immersed in 0.05% $FeCl_2$ or $FeCl_3$ solution and well mixed and immersed for 3 hours. Subsequently, these mixtures were performed in atainles bombe by hydrothermal treatments for 15 hour at 423 K. The obtained products were filtered with Buchner and then sufficiently washed with deionized water and dried at 323 K in an oven. The samples prepared through this process werr characterized with X-ray diffraction technique. The microstructures were observed by SEM.

XANES measurement at P *K*-edge was performed with soft X-ray beam line by a facility of BL-1A station at UV-SOR XANES study was added to clarify the local structure of each atom in the hydroxyapatite structure.

Samples of hydroxyapatite containing Fe^{2+} and Fe^{3+}, which were hydrothermally-treated at 423 K for 15 hours, were evaluated by X-ray diffraction technique. These results of X-ray diffraction suggested that all samples of hydroxyapatite containing Fe^{2+} and Fe^{3+} hydrothermally-treated at 423 K

for 15 hours were identified as hydroxyapatite without other phases. Hydroxyapatite with solid solution of Fe^{2+} and Fe^{3+} prepared by the hydrothermal treatment at 423 K was evaluated by XANES. The result of XANES spectrum at P *K*-edge is shown in Figure 1. Hydroxyapatite containing Fe^{2+} hydrothermally-treated at 423 K shows the same spectrum as a pure hydroxyapatite, which suggest that local structure of PO_4 for hydroxyapatite with Fe^{2+} was seemed to be similar with one of pure hydroxyapatite. On the contrary, the spectrum of hydroxyapatite with Fe^{3+} hydrothermally-treated at 423 K indicates the broad spectrum and no shoulder, comprared to pure hydroxyapatite and hydroxyapatite containing Fe^{2+} hydrothermally-treated at 423 K, that means that local PO_4 structure was distorted with solid solution of Fe^{2+} and Fe^{3+}. Therefore, the local structure of P ions is slightly different between hydroxyapatites treated with the solid solution of Fe^{2+} and Fe^{3+}, the intensity decreased with the incorporation of Fe^{2+} and Fe^{3+}. It could be thought to that this difference of local structure is related with their biocompatibility.

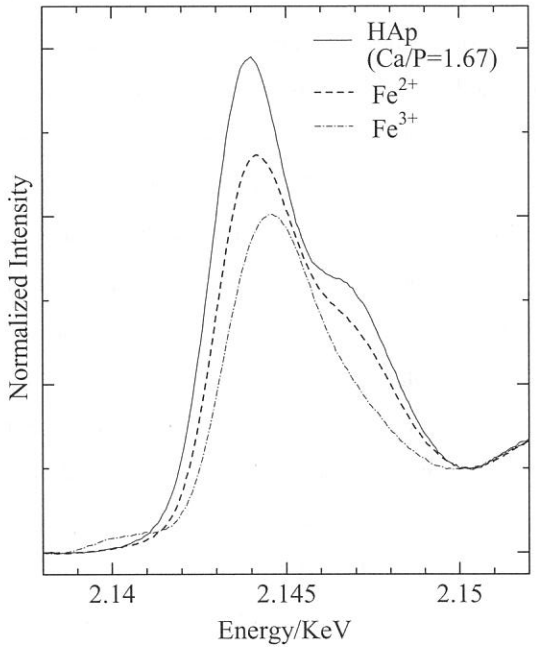

Figure 1 The result of XANES spectrum at P *K*-edge for each hydroxyapatite sample in BL-1A station at UV-SOR. HAp: high pure hydroxyapatite, Fe^{2+}: hydroxyapatite with solid solution of Fe^{2+}, which were hydrothermally-treated at 423 K, Fe^{3+}: hydroxyapatite with solid solution of Fe^{3+}, which were hydrothermally-treated at 423 K.

(BL1A)

Visible and UV Emission Spectra in AlGaN System by the Al-K edge Excitation

S. Naoe, K. Okada[A], S. Hamaura[A], K. Fukui[B], H. Hirayama[C], Y. Aoyagi[C]

Faculty of Engineering, Kanazawa University, Ishikawa 920-1192, Japan

[A]Department of Electric and Electronic Engineering, Fukui University, Fukui 910-8507, Japan

[B]Research Center for Development of Far-Infrared Region, Fukui 910-8507, Japan

[C]The Institute of Physical and Chemical Research

AlGaN System is becoming to important semiconductor material with large band gap energy, where the band gap energy is variable by simply altering the AlGaN composition [1,2]. Total yield spectra and emission spectra in the energy region of visible and ultraviolet light were measured by the Al-K inner core excitation, to clarify the role of Al element on absorption phenomena and on the process to the luminescence. The results will be examined by comparison with the core excitation spectra of another elements of the sample or the spectra of inter band transition.

At BL1A, the absolute photon number of synchrotron radiation light with KTP monochromator crystal is the order of 10^8 /s which will be reduced to 10^6 /s at the input of measuring circuits instrument on the measurement of absorption spectra. Therefore, it is difficult to get the enough signal intensity on measuring the secondary process such as luminescence, by using photomultiplier on the normal mode to catch the signal current flow directly. We have developed a spectroscope system catching light by CCD block cooled at liquid nitrogen temperature. The luminescence light from the sample is gathered by a quartz optical fiber inserted into a vacuum sample chamber. The position of the tip of the optical fiber is variable by an external manipulator system. The measurements were carried out at the separation of about 1cm between the center of the sample and the tip of the optical fiber. The separation is the limit length unless the fiber becomes cutting the incident synchrotron light beam on the sample.

In doped AlGaN sample is known as the most luminosity sample where In takes place of the role of the sensitized center of luminescence. The efficiency of luminescence increases usually in proportional as lowering temperature. The sample was set on copper sample holder of liquid He flow type cryostat. The sample holder was glued onto a sapphire plate glued also onto the cooling head of the cryostat to make measurements of the total yield spectra of photoelectron. The photoluminescence spectra were measured at about 20 K by Al-K inner core excitation in $In_{0.05}Al_{0.20}Ga_{0.75}N$ sample. The obtained luminescence spectra are shown in Figure 1 with the spectra of the case of inter band excitation for the comparison each other in the energy region of visible and UV light. The luminescence spectra are composed of a sharp blue emission band (B-emission, 3.65 eV) and a broad yellow band (Y-emission, 2.25 eV).

The absorption spectra of the Al-K inner core excitation were obtained by measuring the total yield spectra of photoelectron. The yield spectra measured at room temperature are shown in Figure 2 , where the outline of the yield spectra are inserted into the figure for the comparison with the excitation spectra of photoluminescence. The height of the main peak of yield spectra amounts to several picoampere of signal current giving good quality of spectra. The excitation spectra of photoluminescence are generally obtained from the recording of the intensity of luminescence as a function of excitation light energy, by continuously driving the scanning mechanism of crystal monochromator at

BL1A beam port. In our case, the luminescence spectra must be measured at a stop to scan the monochromator for each energy position of excitation light. A problem would occur on the reproducibility of the precise energy position of excitation light on the step by step measuring. Fig.2 (a) and (b) shows the obtained excitation spectra of Y- and B-emission bands, respectively. The result shows that the reproducibility of energy position of monochromator is not matter and that the excitation spectra can correspond to the yield spectra in Al-K edge region.

As the result of our measurements, the photoluminescence spectra are just about similar to each other between Al-K inner core excitation and inter band excitation. It will lead to the next step of our study that the peak position of B emission band excited on Al-K core region occupies on the higher energy position than that of B emission band excited on inter band region.

References

[1] S. Strite and H. Moroc : J. Vac. Sci. Technol. B **10** (1992) 1237.

[2] B. Monemar : Material Science and Engineering B **59** (1999) 122.

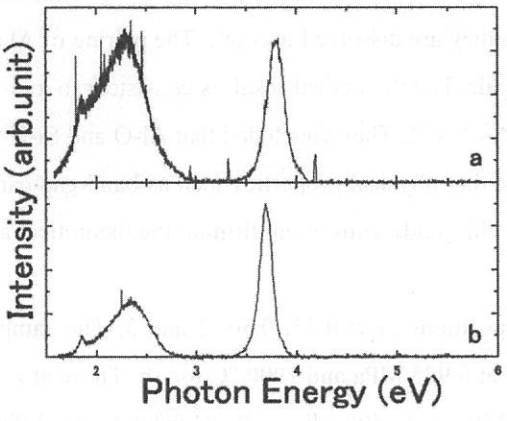

Fig.1 Photoluminescence spectra in $In_{0.05}Al_{0.20}Ga_{0.75}N$ excited by the light of Al-K edge (a) and by that of inter band Transition (b).

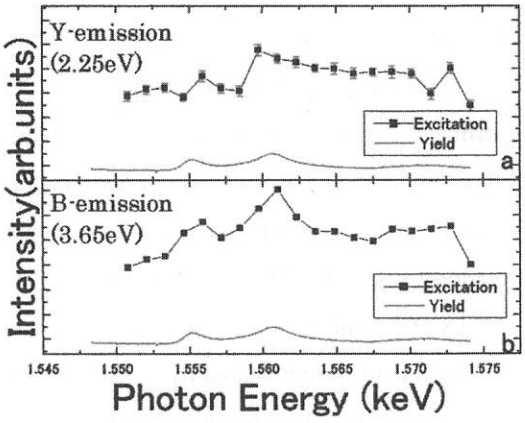

Fig. 2 Excitation spectra of Photoluminescence of Y and B emission.

(BL1A)

Atomic structures of β-SiAlONs by Al-K XANES

Kazuyoshi TATSUMI, Teruyasu MIZOGUCHI, Satoru YOSHIOKA, Masahiro KUNISU, Masato YOSHIYA, Isao TANAKA and Hirohiko ADACHI

Department of Materials Science and Engineering, Kyoto University, Sakyo, Kyoto, Kyoto 606-8501 Japan

Solid solution ceramics are widely utilized in modern technology. However, their atomic and/or electronic structures have not been fully clarified in most of the cases. SiAlONs in the Si_3N_4-AlN-Al_2O_3-SiO_2 ceramic system are one of them. They are solid solutions of α- and β-Si_3N_4 in which Al and O atoms substitute the Si and the N sites. Their chemical formula is usually represented as $Si_{6-z}Al_zO_zN_{8-z}$. Their mechanical properties such as elastic constants are known to be modified according to the solution,[1] which is utilized in a variety of engineering applications. The mechanism behind the solution effects is strongly related to the distribution of the solute atoms. However, only little is known about the distribution.

We have recently examined first principles energetics on the substitutions in β-phase.[2] We found that the solutes prefer to be bound at the nearest neighbor sites when they are dissolved in Si_3N_4. The pairing of Al and O atoms made energy gain of a few tenth of eV per an Al-O pair. The theoretical result is consistent to a previous experimental study by Dupree *et al.*[3] using ^{27}Al and ^{29}Si MAS-NMR. They concluded that Al-O and Si-N bonds are predominant. Our theoretical calculations also suggested that physical properties such as band-gap can only be explained when such pairing is fully taken into account. This study aims at confirming the theoretical atomic structures of SiAlONs by XANES spectra.

SiAlON samples were prepared with systematic compositions of z=0.23, 0.50, 2 and 3. The samples at z=0.23 and 0.50 were prepared by N_2 gas-pressure sintering at 0.925 MPa and 1900 °C for 1h. Those at z=2 and 3 were prepared by hot isostatic pressure sintering at 160 MPa and 1500 °C for 3h. Powder X-ray diffraction experiments confirmed no crystalline phases other than β. Al-K XANES were collected in a total electron yield mode at room temperature using a KTP two-crystal monochrometer at BL1A of the UVSOR.

Figure 1 shows the experimental Al-K XANES from β-SiAlONs and from their referential compounds (α-Al_2O_3 and wulzite-AlN (w-AlN).) Two points are noteworthy from Fig. 1. Firstly, the spectral shapes of SiAlONs are almost the same for all the compositions. This suggests that local environments of Al are similar from z=0.23 to z=3. Secondly, a clear chemical shift among w-AlN, a-Al_2O_3 and SiAlONs is found. The 1st peaks of SiAlONs are located at the middle of those of w-AlN and α-Al_2O_3.

For interpretation of the chemical shift, the theoretical and the experimental spectra of SiAlONs are compared in Fig. 2. The theoretical spectra were obtained using first principles OLCAO method[4] using supercells composed of 42 atoms. Atomic structures were optimized in our previous work by a plane wave pseudopotential method.[2] The OLCAO calculations were made for 45 kinds of Al sites in 17 kinds of models. The 45 spectra are classified and averaged according to the local coordinations. Figure 2 shows five theoretical spectra of Al coordintated by four N (AlN_4), three N and one O (AlN_3O), two N and two O (AlN_2O_2), one N and three O ($AlNO_3$), and four O (AlO_4). We have also calculated spectra from the referential compounds, w-AlN

and α-Al_2O_3 (They are not presented in this report.). These results showed quantitative reproduction of the experimental chemical shift within an accuracy of < 0.1 eV. In Fig. 2, we calibrated the theoretical energy in such a way that the 1st peak of α-Al_2O_3 of theoretical spectra is set at the experimental spectrum.

The experimental 1st peak of SiAlON is located in between those of the theoretical spectra of AlO_3N and AlO_4 independent of z-values. This indicates that Al solutes in SiAlONs are coordinated preferentially by O solutes. This is consistent with Dupree's NMR analysis and our previous theoretical results. The good agreement between the theoretical and the experimental spectra confirms the validity of our theoretical atomic and electronic structures of SiAlONs.

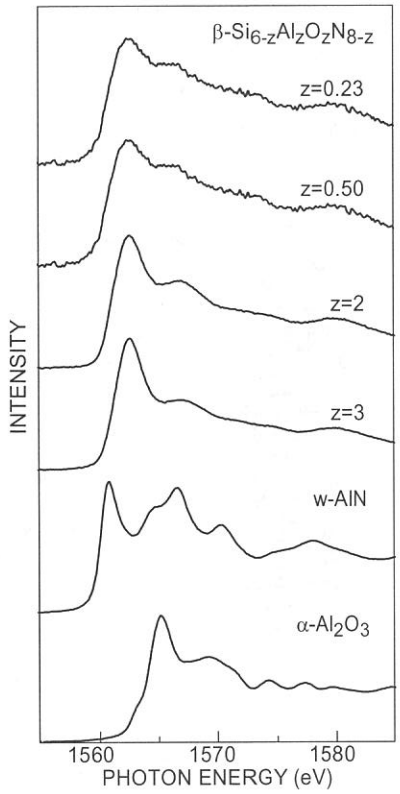

Fig1. Experimental Al-K XANES from β-SiAlONs and references.

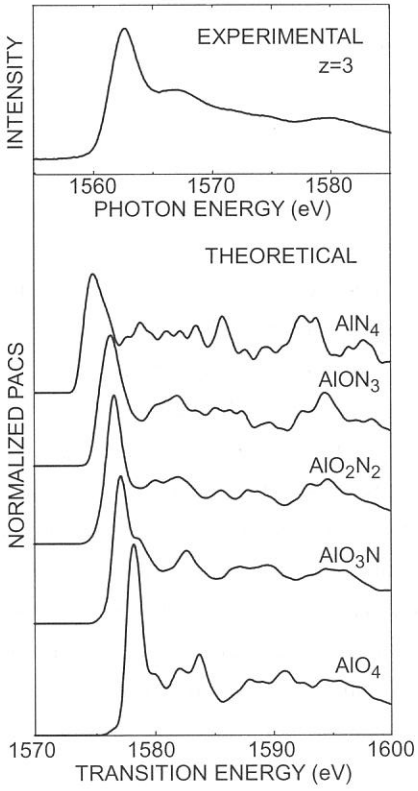

Fig.2 Comparison between the experimental and the theoretical Al-K XANES from SiAlONs.

Acknowledgements This work was supported by the grant-in-aid for priority area (No. 751) from MEXT of Japan. KT is supported by JSPS research fellowship. Helps in sample preparation by Dr. N. Hirosaki and Dr. Y. Yamamoto are gratefully acknowledged.

REFERENCES

1. I. Tanaka, S. Nasu, H. Adachi, Y. Miyamoto and K. Niihara, Acta metall. mater., **40** 1995 (1992).
2. K. Tatsumi, I. Tanaka, H. Adachi and M. Yoshiya, Phys. Rev. B, **66** 165210 (2002).
3. R. Dupree, M. H. Lewis and M. E. Smith, J. Appl. Cryst., **21** 109 (1988).
4. Shang-Di Mo and W. Y. Ching, Phys. Rev. B, **62** 7901 (2001).

(BL4B)

Electronic structure of DNA under the chemical-doping condition probed by PES and NEXAFS

Masashi Furukawa (†, ‡), H. S. Kato (†), M. Taniguchi (#), T. Hatsui (§), N. Kosugi (§, ß), T. Kawai (‡, #) and Maki Kawai (†)

† *RIKEN (The Institute of Physical and Chemical Research), Wako, Saitama 351-0198, Japan*
‡ *The Institute of Scientific and Industrial Research (ISIR), Osaka University, Ibaraki, Osaka 567-0047, Japan*
# *Nanoscience and Nanotechnology Center, ISIR, Osaka University, Ibaraki, Osaka 567-0047, Japan*
§ *Institute for Molecular Science (IMS), Myodaiji, Okazaki 444-8585, Japan*
ß *Ultraviolet Synchrotron Orbital Radiation (UVSOR) Facility, IMS, Myodaiji Okazaki 444-8585, Japan*

During the last several years, the carrier transport measurements through DNA (Fig. 1) between nm-spaced electrodes have been discussed without the understanding of their electronic structures near the Fermi level (E_F), giving rise to the proposal of controversial properties –from a good conductor to an insulator–. We believe so far, the concept of carrier doping into DNA is the promising aspect for the control of its electrical properties since VIS/UV absorption data tell us that its HOMO–LUMO gap is ≤ 5 eV (λ_{max} ~260 nm). Actually, the theoretical and experimental (mainly *I–V* characteristics) reports have told us that these properties depend on not only the base sequence but also the chemical species surrounding DNA (e.g., H^+, counterion). Of special interest topics here are that their properties can be controlled *via* artificial carrier-doping such as 'electric-field-doping' [1] and also 'chemical-doping' with iodine [2], in which well-defined sequence of DNA polynucleotides, Poly(dG)·poly(dC) (***GC***), clearly showed the hole-conductive behavior. Here we show the electronic structure of ***GC*** together with Poly(dA)·poly(dT) (***AT***),under the iodine-doping (hole-doping) condition, using PES and NEXAFS, in order to evaluate the iodine-doping effect into them and to discuss their conduction mechanism. We prepared ***GC***- and ***AT***-based DNA film coated on SiO_2/*p*-Si(111) substrate, the thickness of which is estimated to be 100–200 nm. The chemically-doped material used here was prepared from a two-zone reaction set-up using a quartz ampoule loaded with DNA film and a previously degassed iodine, evacuated at room temperature to 10^{-5} Torr order, sealed and held for 10 hours. PES and NEXAFS measurements were performed at BL4B, in which the endstation (UHV system) is equipped with electron energy analyzer Scienta SES200 and a retarding-field electron detector for NEXAFS.

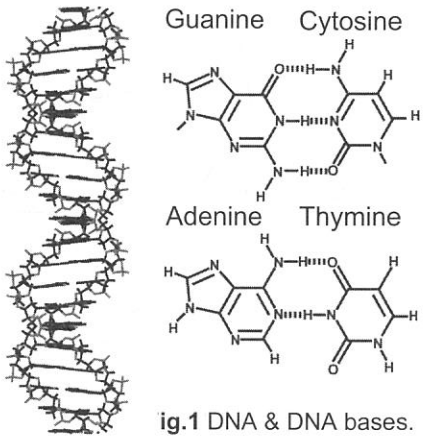

ig.1 DNA & DNA bases.

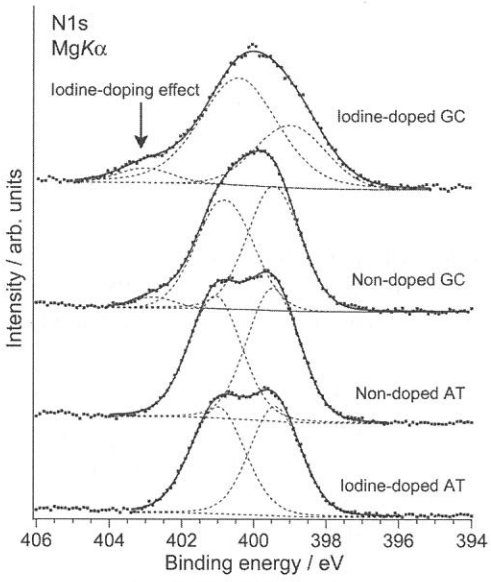

Fig.2 N1s XP spectra

Figure 2 shows the N 1s XP spectra for iodine-doped and non-doped ***GC*** and ***AT*** films. Two major peaks were obtained, which were ascribed to imine (–N=) below binding energy (B.E.) of 400 eV and amine (–NH–) below 401 eV, respectively. After doping with iodine into ***GC***, the intensity of cationic radical peak (B. E. : 402–404 eV) was increased, while that for imine products was drastically decreased. The iodine-doping effect in ***GC*** is therefore described as follows: the doped iodine is localized at the imine units and changes it into cationic radicals. This behavior is quite similar to the polyaniline case [3], which behaves as an excellent conductor after anion-doping process. In this situation, we have also observed valence band region, using PES ($h\nu$ = 170 eV), as shown in Fig. 3. The spectra for ***GC*** and ***AT*** can be divided into two intense peaks: one is located around 6 eV (π chracter), and the other is around 10 eV (π and σ character). The whole structure for both non-doped ***GC*** and ***AT*** are not so drastically different from each other, however, the interesting behavior here is that the iodine-doping effect into ***GC*** and ***AT*** showed the quite opposite behavior: the edge of spectrum and/or valence band maximum (VBM) for ***GC*** case seems to be shifted toward the E_F. Unoccupied electronic states of nitrogen *K*-edge for these samples have also been observed as shown in Fig. 4. The characteristic resonance peaks are due to the excitations from N 1s to $\pi^*_{-N=}$ (photon energy of 399–401 eV), π^*_{-NH-} (401–404 eV), and σ* (above 405 eV) states. The absence of shifts in the continuum σ* resonance suggests that the bond lengths and thus π conjugated ring structure do not change during the doping process. The density of unoccupied states near E_F as derived from N *K*-edge were also influenced by iodine-doping especially for ***GC***, in which the intensity of first π* transition is reduced a little and this seems to be accompanied with the appearance of new empty states below its $\pi^*_{-N=}$ states. The behavior of electronic structures around E_F especially for ***GC*** has a good agreement with the fact that the electrical conductivity clearly increases due to the hole-doping, and is the quite same as π-conjugated conductive polymer such as polypyrrole and polythiophene, both in which the formation of polaron (radical cation) states between their midgap states has been expected to be a dominant role for their carrier conduction. The theory of 'polaron-hopping through DNA' has actually been given by Conwell et al., and it is often accepted based on the carrier *transfer* and *transport* measurements, in which 'polaron-hopping' fittings were applied to the *I-V* characteristic data. On the other hand, our spectroscopic study supports these predictions more directly, because N 1s core level data have clearly indicated the existence of cationic phase at the nitrogen site (N^+) due to the hole-doping (Fig. 2) in addition to the behavior around E_F (Figs. 3 and 4).

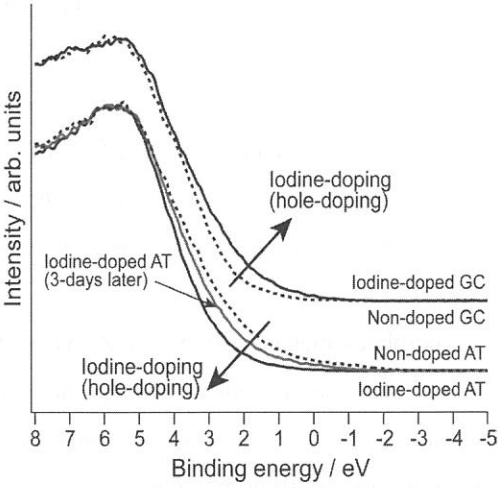

Fig.3 Valence band spectra

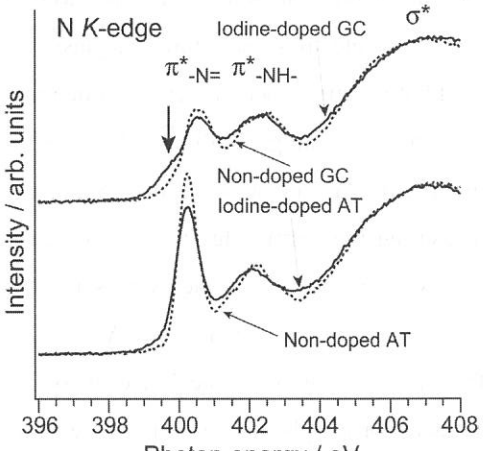

Fig.4 N *K*-edge NEXAFS spectra.

References

[1] K. –H. Yoo *et al.*, *Phys. Rev. Lett.* **87,** 198102 (2001).

[2] M. Taniguchi *et al.*, *Jpn. J. Appl. Phys.* **42,** L215 (2003).

[3] X. –R. Zeng *et al.*, *J. Poly. Sci.* **35,** 1993 (1997).

(BL5A)

Electronic Structure of Bulk Glassy $Zr_{55}Al_{10}Cu_{30}Ni_5$ Alloy

Y. Morishita, K. Shimba, H. Murayama, M. Kato, S. Yagi, T. Takeuchi,* U. Mizutani, T. Zhang,**
M. Hasegawa,** A. Inoue,** and K. Soda

Graduate School of Engineering, Nagoya University, Furo-cho, Chikusa-ku, Nagoya 464-8603
**Research Center for Advanced Waste and Emission Management, Nagoya University, Furo-cho, Chikusa-ku, Nagoya 464-8603*
***Institute for Materials Research, Tohoku University, Katahira, Aoba-ku, Sendai 980-8577*

Amorphous metals, particularly Zr-based bulk glassy alloys, have drawn much attention as new materials which possess useful engineering properties such as high mechanical strength, good ductility, and high corrosion resistance [1, 2]. Although the electronic structure of Zr-based glass alloys has been studied in relation to their high ability of absorbing hydrogen [3], the origins of the large glass formation ability and unique properties of the bulk glassy alloys have not been well understood from the microscopic point of view yet. Thus we have studied the electronic structure of a glassy $Zr_{55}Al_{10}Cu_{30}Ni_5$ alloy by photoelectron spectroscopy as the first step.

Photoelectron spectra were recorded under an ultrahigh vacuum of 1.5×10^{-8} Pa at room temperature with a hemispherical energy analyzer (Omicron EA125) at BL5A of UVSOR. Total energy resolution including the thermal broadening was set to 0.15~0.2 eV at the photon energy $h\nu$ of 30~130 eV, which was confirmed by measuring the Fermi edge in the photoelectron spectra of an evaporated Au film. The origin of the binding energy E_B, *i.e.* the Fermi energy, was also determined by the Fermi edge of the Au film.

An ingot of a bulk glassy $Zr_{55}Al_{10}Cu_{30}Ni_5$ alloy was prepared by a casting method [2]. Specimens were cut from the ingot into a typical size of 3x3x2 mm^3 and attached on a cupper plate by conductive glue. Clean surfaces for the photoelectron measurement were obtained by *in situ* scraping the specimen with a diamond file or sputtering them with 0.5 keV Ar^+ ion beam.

Figure 1 (a) and (c) show X-ray diffraction patterns of the inner bulk part and outer surface part of the ingot, respectively, after cutting the ingot. Broad halo features in Fig.1 (a) reveal the glassy state of the bulk specimen [1], while sharp peaks in Fig.1 (c) are indicative of the crystallization in the surface region of the ingot. As seen in Fig.1 (b), almost no change in the diffraction pattern was recognized after the photoelectron measurement. This indicates that the clean surface preparation and the photoelectron measurement do not affect the glassy state of the specimen.

Figure 2 shows typical valence-band photoelectron spectra of the bulk glassy $Zr_{55}Al_{10}Cu_{30}Ni_5$ alloy. In the figure, a spectrum recorded by the use of a He I ($h\nu$ = 21.2 eV) light source and a photoelectron spectrometer (Omicron AR65) in our laboratory is also shown for comparison, and the intensity is normalized at E_B ~3.7 eV (the feature C below). In these spectra, there are four features recognized; A at E_B ~0.6 eV, B at ~2.0 eV, C at ~3.7 eV, and D at ~6.1 eV. Since the feature D was increased in prolonged measurement, it is attributed to the O 2*p*-derived states, but unfortunately it could not be removed completely in the present measurement. The feature A is ascribed to the Zr 4*d* states, because it shows a maximum at $h\nu$ ~ 40 eV and decreases as the

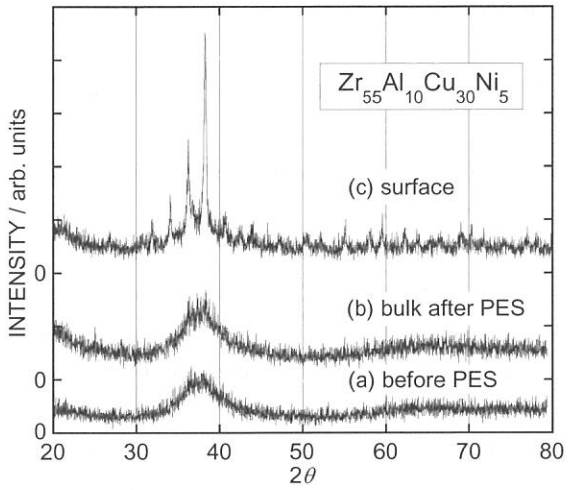

Fig.1 X-ray diffraction patterns for the inner bulk part, (a) and (b), and outer surface one (c) of the ingot of the bulk glassy $Zr_{55}Al_{10}Cu_{30}Ni_5$ alloy.

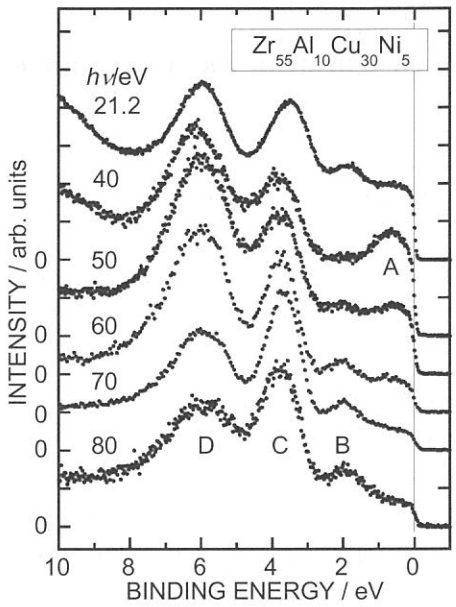

Fig.2 Valence-band photoelectron spectra of the bulk glassy $Zr_{55}Al_{10}Cu_{30}Ni_5$ alloy. The excitation photon energy $h\nu$ is indicated in the figure.

excitation photon energy is increased, which indicates the Cooper minimum of the Zr 4*d* photoionization process [4]. The features B and C are ascribed to the Ni 3*d* and Cu 3*d* states, respectively, because the constant initial state spectra of these features show the 3*p*-3*d* resonance behavior around these 3*p* thresholds [5].

Remarkable feature of the observed photoelectron spectra is the highly symmetric spectral shape of the transition metal *d* bands with high binding energy and narrow width in comparison with the *d* bands of the crystalline transition metals. The Cu and Ni 3*d* band widths decrease from ~2 eV for crystalline Cu and Ni metals to ~1 eV for the glassy alloy, which is mainly due to the reduction in the neighboring atoms to hybridize with those transition metals in the glassy alloy. The symmetric shape may also arise from the lack of the crystalline periodicity. At present, however, it is not clear whether these aspects are intrinsic for the glassy states of this alloy or not. Further study is intended on the crystalline counterpart and the glassy alloys with different compositions. The surface effects may be also anticipated to affect the spectrum, since the peak of the *d* bands is slightly shifted to the low binding energy side at $h\nu = 21.2$ eV, where the photoelectron escape depth will increase in comparison with $h\nu \sim 60$ eV [6]. The oxygen contamination will be removed or suppressed on the measurement at low temperatures.

References

[1] A. Inoue and T. Zhang, Mat. Trans. JIM **37** (1996) 185.

[2] A. Inoue, Y. Kawamura, T. Shibata, and K. Sasamori, Mat. Trans. JIM **37** (1996) 1337.

[3] G. Petö, I. Kakonyi, K. Tompa, and L. Guczi, Phys. Rev. B **52** (1995) 7151.

[4] J. J. Yeh and I. Lindau, Atom. Data Nucl. Data Tables **32** (1985) 1.

[5] L. C. Davis, J. Appl. Phys. **59** (1986) R25.

[6] S. Tanuma, C. J. Powell, D. R. Penn, Surf. Interface Annual., **17** (1988) 911.

(BL-5A)

Synchrotron-radiation photoemission study of dodecanethiolate-passivated Au nanoparticles

Akinori Tanaka[A], Yuitsu Takeda[A], Tazumi Nagasawa[A], Masaki Imamura[A], and Kazutoshi Takahashi[B]

[A]*Department of Physics, Graduate School of Science, Tohoku University, Aoba-ku, Sendai 980-8578, Japan*
[B]*UVSOR Facility, Institute of Molecular Science, Okazaki, Aichi 444-8585, Japan*

Metallic nanoparticles are attracting much interest because of their distinctive physical and chemical properties found in neither bulk nor molecular/atomic systems, such as high catalytic activity and Coulomb blockades. Recently, the surface-passivated nanoparticles have been chemically synthesized in the solution including surfactants. These surface-passivated nanoparticles are monodisperse and very stable even at room temperature. Furthermore, these surface-passivated nanoparticles exhibit closed-packed nanoparticle self-assemblies on single-crystalline substrates, and therefore, it is considered that they could be important constituents of future nanostructured devices. In order to elucidate their intriguing properties and to develop future devices, it is indispensable to characterize the chemical states of these surface-passivated nanoparticles. In this work, we have carried out a photoemission study of dodecanethiolate (DT)-passivated Au nanoparticles in order to investigate the chemical states of surface-passivated Au nanoparticles.

The DT-passivated Au nanoparticles were synthesized by a two-phase reduction method. The detailed procedure has been described elsewhere [1, 2]. Photoemission measurements were carried out at BL-5A of UVSOR Facility, Institute for Molecular Science. For the photoemission measurements, the synthesized DT-passivated Au nanoparticles were supported on HOPG substrates by evaporating the solvent (toluene) from the dispersion of DT-passivated Au nanoparticles on the HOPG cleaved surface in a nitrogen-filled glove bag directly connected to the photoelectron spectrometer. Then the samples were transferred into the photoemission analysis chamber without exposure to air. Photoemission measurements were performed using EA-125HR (OMICRON Co.) photoelectron spectrometer with the incident photon energy of 180 eV. The photoemission spectra were recorded at room temperature, and no degradation of the samples was observed.

Figure 1 shows the TEM micrographs and the corresponding size distributions in diameter obtained by TEM observations for the DT-passivated Au nanoparticles used in this work. The obtained mean diameters d_m are 2.6, 3.0, 4.9, and 5.2 nm. An important point to note is that each nanoparticle is well separated from its neighboring nanoparticles, indicating that the present Au nanoparticles are well surface-passivated by the dodecanethiol molecules. Figure 2 shows the Au $4f_{7/2}$ core-level photoemission spectra of the DT-passivated Au nanoparticles with the various diameters on the HOPG substrates, compared with that of bulk Au polycrystalline evaporated film. As shown in Fig. 2, the DT-passivated Au nanoparticles exhibit the significant higher-binding-energy shifts of Au $4f$ core-level spectra, compared with the bulk Au crystallite. Furthermore, the binding energies of Au $4f$ core-level spectra shift to a higher-binding-energy side with decreasing the nanoparticle diameter. These energy shifts are considered to originate from the final-state effect in the photoemission. This discussion is described in detail elsewhere [1, 2]. In addition, Au $4f$ core-level spectra of the DT-passivated Au nanoparticles exhibit a slightly asymmetric peak with a tail at the higher-binding-energy side, and this asymmetry increases with decreasing the nanoparticle diameter. The results of line-shape analyses of Au $4f_{7/2}$ core-level spectra for bulk Au crystallite and DT-passivated Au nanoparticles with various mean diameters are also shown in Fig. 2. As previously well established, we decomposed the Au $4f$ core-level spectrum of bulk Au crystallite into two components, which originate from the Au atoms in the bulk and topmost surface Au layer. The higher-binding-energy (dotted line) and lower-binding-energy (short broken line) peaks are bulk and surface components, respectively. On the other hand, it is found that the Au $4f$ core-level photoemission spectra of the

DT-passivated Au nanoparticles are also reproduced by two components and that the relative intensity of two-components depends on the nanoparticle diameter. That is, the relative intensity of higher-binding-energy component (long broken line in Figs. 2(b)-(e)) to lower-binding-energy component (dotted line in Figs. 2(b)-(e)) increases with decreasing the nanoparticle diameter. The nanoparticle has a higher number ratio of surface atoms to atoms in bulk with decreasing the nanoparticle diameter. Furthermore, the binding energy and spectral feature of the lower-binding-energy component in each sample are similar to those of bulk component in the Au 4*f* core-level spectrum observed for bulk Au crystallite. Therefore, it is considered that the lower-binding-energy and higher-binding-energy components originate from the inner Au atoms of Au nanoparticles and the surface Au atoms of Au nanoparticles bonded to surface-passivants of DT molecules, respectively. An important point to note is that these surface components accompany with chemical shifts to higher binding energies relative to the bulk components. This indicates the different chemical states in the surface Au atoms bonded to DT molecules with the inner Au atoms and existence of a chemical reaction (chemisorption) between the surface-passivants of DT molecules and Au nanoparticles. The chemical shifts of DT-passivated Au nanoparticles with the mean diameters of 5.2, 4.9, 3.0, 2.6 nm are 0.27, 0.27, 0.28, and 0.33 eV, respectively. The chemical shifts of surface Au atoms bonded to DT molecules increase with decreasing the nanoparticle diameter. This indicates that the bonding nature between the surface-passivants of DT molecules and Au nanoparticle surface, such as a coordination number and configuration of surface-passivants, changes with the nanoparticle diameter. The above dependence of bonding nature on the nanoparticle diameter might originate from the structural factor such as size-dependent curvature of nanoparticle surface, effect due to the existence of habit in the smaller nanoparticles, *etc*.

References

[1] A. Tanaka, Y. Takeda, T. Nagasawa and S. Sato, Phys. Rev. B **67**, 033101 (2003).

[2] T. Nagasawa, A. Tanaka, H. Sasaki, Y. Kuriyama, S. Suzuki, and S. Sato, Mat. Res. Soc. Symp. Proc. **704**, 319 (2002).

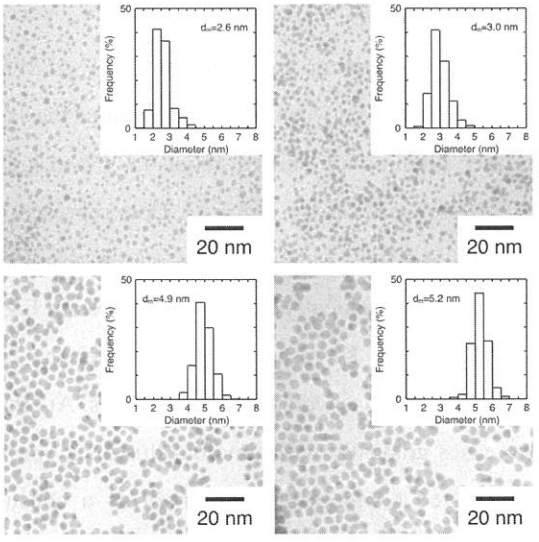

Fig. 1. TEM micrographs and size distributions in the diameter of DT-passivated Au nanoparticles with mean diameters d_m of 2.6 nm, 3.0 nm, 4.9 nm, and 5.2 nm.

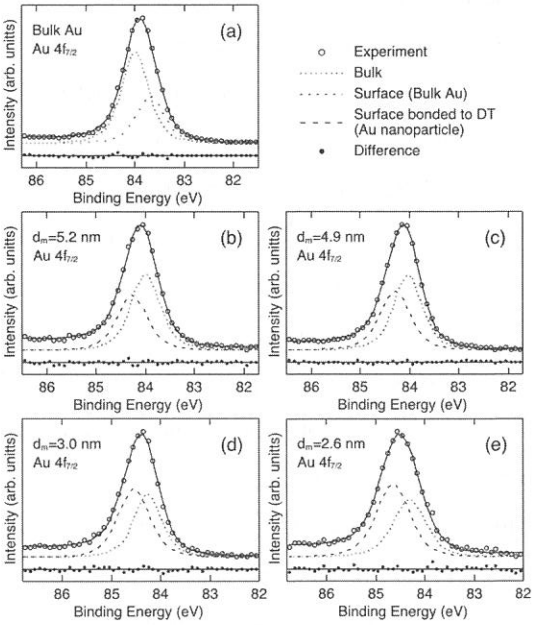

Fig. 2. Results of line-shape analyses for Au $4f_{7/2}$ core-level photoemission spectra of (a) bulk Au crystallite, and DT-passivated Au nanoparticles with mean diameter d_m of (b) 5.2 nm, (c) 4.9 nm, (d) 3.0 nm, and (e) 2.6 nm. The spectrum of bulk Au crystallite is decomposed into bulk (dotted line) and surface (short broken line) components, and those of DT-passivated Au nanoparticles are decomposed into bulk components (dotted lines) and surface components bonded to surface DTs (long broken lines). The bottom of each panel is the difference between the observed spectrum and the sum of the decomposed components.

(BL5A)

Temporal Change of Surface Photovoltage Effects in *p*-type GaAs Studied with Photoelectron Spectroscopy Using SR and Laser

Senku TANAKA [†], Kazutoshi TAKAHASHI [A ‡], Junpei AZUMA [B] and Masao KAMADA [B]

The Graduate University for Advanced Studies, Okazaki 444-8585

[A] *UVSOR Facility, Institute for Molecular Science, Okazaki 444-8585*

[B] *Synchrotron Light Application Center, Saga University, 840-8502*

When the light with photon energies larger than the width of the bulk band-gap is absorbed, electron-hole pairs are generated. The photo-generated carriers are spatially separated toward surface and bulk by the electric field in the surface space charge region (SCR). This charge separation generates electromotive force, so-called surface photovoltage (SPV). It has been pointed out that the SPV effect is considerable matter to develop the new generation of spin-polarized electron sources [1]. In this report, we present the temporal change of the SPV effects in *p*-type GaAs caused by laser illumination. The variation of the SPV in the time domain of microseconds, which was investigated by the photoelectron spectroscopy using synchrotron radiation and laser, and the annihilation mechanism of the SPV are discussed.

Experiments were performed at BL5A. A Zn doped (1×10^{19} cm^{-3}) *p*-type GaAs was used for the measurements. We used the Ti: Sapphire laser (COHERENT Mira 900-F) and the regenerative amplifier (COHERENT RegA) as the excited light sources to cause the SPV effects. The RegA laser system was set to provide 1.55 eV and 10 kHz pulses with about 20mW. The OMICRON electron-energy analyzer (EA-125HR) was used to observe the photoelectron spectra. The SPV effects caused by laser illumination have been observed via core-level photoelectron spectra [2, 3]. The temporal overlap of the laser and SR pulses was evaluated by an MCP-PM/TAC system. The spatial overlap was carefully checked by our eyes.

The Ga-*3d* photoelectron spectra with and without the laser illumination are shown in Fig. 1. At 295 K, no obvious difference is clearly appreciable on the photoelectron spectra between with and without the laser illumination. At 90 K, the photoelectron spectrum with the laser illumination shifted about 0.3 eV to higher kinetic energies. The temporal changes of the SPV at 295 K and 90 K are shown in Fig. 2. Dots represent the SPV values obtained from the change in the photoelectron intensity at a fixed kinetic energy, on the assumption that the spectral shape of the core-level photoelectrons does not change drastically with time. As seen in Fig. 2, the peaks of about 0.175 V and 0.45 V are observed at 295 K and 90 K, respectively, just after the laser excitation. Apparently, the sample temperature affects the temporal profiles as well as the SPV values. At 295 K, the SPV disappears within about 1 μs. At 90 K, the SPV decreases gradually with time but this decay profile cannot be fitted with a single-exponential curve. The accumulated component is observed as a constant background of about 0.25 V, which originates from the residual SPV produced by a train of laser pulses.

[†] present address : Research Center for Materials Science, Nagoya University, Nagoya 464-8602

[‡] present address : Synchrotron Light Application Center, Saga University, 840-8502

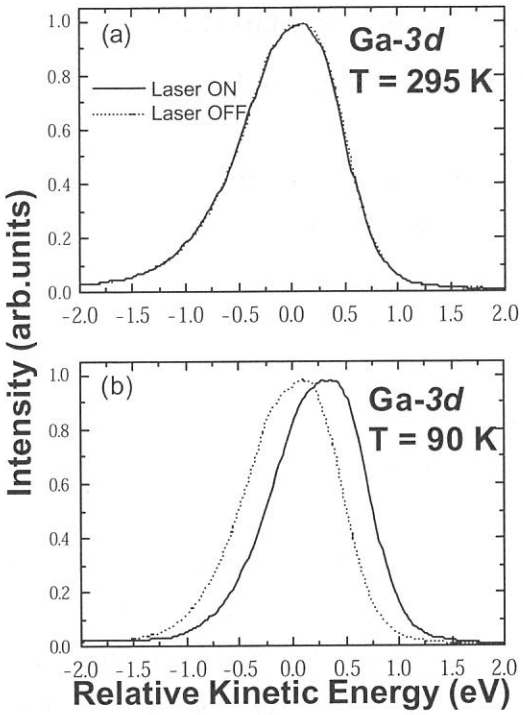

Figure 1. The Ga-3d core-level photoelectron spectra at (a) 295 K and (b) 90 K in the clean surface of *p*-GaAs (100). Solid and dotted lines represent the spectra with and without laser excitation, respectively.

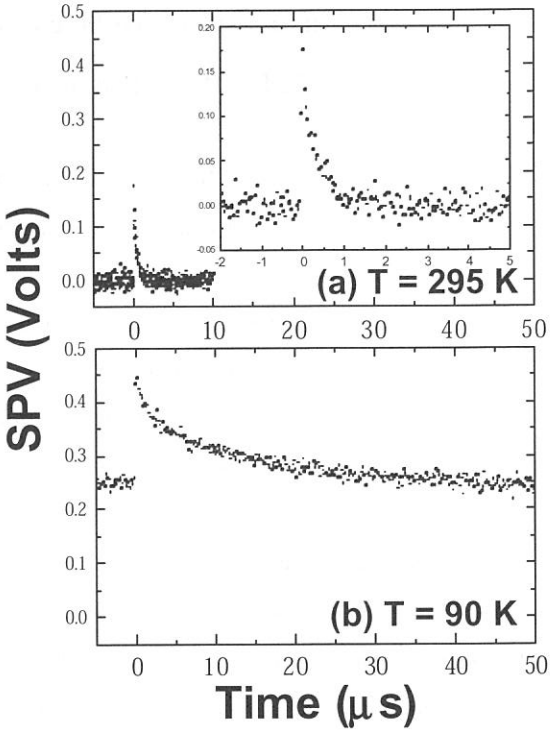

Figure 2. (a) Temporal profile of SPV in the *p*-type GaAs at 295 K. (b) Temporal profile of SPV in the *p*-type GaAs at 90 K.

The lifetime of the SPV depends on the lifetime of the recombination of the surface electrons and bulk holes in the case of a *p*-type semiconductor. In order to recombine with the surface electrons, the holes must pass through the potential barrier in the surface SCR. Two ways to pass through the potential barrier shall be considered. One is the thermionic way and the other is the tunneling one. The amount of the excess surface charge Δp can be written as

$$\Delta p(t) = \Delta p_0 - Q_{thermionic}(t) - Q_{tunnel}(t), \quad (1)$$

where Δp_0 is the amount of the initial excess charge just after the laser excitation, $Q_{thermionic}$ and Q_{tunnel} is the thermionic and the tunneling recombination charge, respectively. Obviously, both the value of $Q_{thermionic}$ and Q_{tunnel} depend on the temperature and the shape of an energy barrier (i.e., the shape of SCR). If the quantity of Q_{tunnel} would be much larger than that of $Q_{thermionic}$, the lifetime of the SPV should be similar at 295 K and 90 K. As seen in Fig. 1, the SPV effect is dominant at 90 K, but not appreciable at 295 K. It is expected from this result that the thermionic recombination process is dominant at 295 K, resulting in the suppression of the SPV. The numerical calculation supported this expectation quantitatively at 295 K and qualitatively at 90K. It is concluded that the thermionic recombination is the dominant process at 295 K, while the tunneling recombination becomes appreciable at 90 K [4].

References

[1] T. Nakanishi, *14th. Int. Spin Phys. Symp.* AIP conf. proc. **570**, 274 (2001).

[2] S. Tanaka et al., Phys. Rev. B **64** (2001) 155308.

[3] S. Tanaka et al., UVSOR Activity Report, 2000, 152.

[4] S. Tanaka et al., J. Phys. Soc. Jpn., **72**, 659 (2003).

(BL5A)

Surface-photovoltage effect in GaAs-GaAsP superlattices studied with combination of synchrotron radiation and laser

Senku TANAKA[†], Tomohiro NISHITANI [A], Tsutomu NAKANISHI [A]
Kazutoshi TAKAHASHI [B‡], and Masao KAMADA [C]

The Graduate University for Advanced Studies, Okazaki 444-8585
[A] Department of Physics, Nagoya University, Nagoya 464-8602
[B] UVSOR Facility, Institute for Molecular Science, Okazaki 444-8585
[C] Synchrotron Light Application Center, Saga University, Saga 840-8502

The negative electron affinity (NEA) surfaces of p-type GaAs and its superlattice (SL) have been attracting much interest, since they are useful as polarized electron sources with high quantum yield and high degree of spin-polarization. Gómez *et al.* [1] have proposed that the surface photovoltage (SPV) effect plays an important role in causing the saturation problem on the extracting of spin-polarized electrons. Recently, Togawa *et al.* [2] demonstrated that the SL photocathode is one of the most favorable spin-polarized electron sources since it has high spin-polarization and the potential for producing a multi-bunch electron beam. It has been supposed that the SL photocathode can suppress the saturation of the photo current because of the small SPV effect. The purpose of this work is to confirm the SPV effect in the SL photocathode from a viewpoint of basic surface science. We measured the SPV effects and its time dependence in GaAs-GaAsP SL by means of core-level photoelectron spectroscopy with combination of SR and laser.

The experiment was performed at the BL 5A. Two kinds of GaAs-GaAsP SL (named as SL #1 and SL #16) were studied in the present experiments. They have been fabricated at Daido Steel Co. Ltd. and Nagoya Univ., respectively, using the MOCVD method. The parameters of the SL #1 and SL #16 are summarized in Table I, where the quantum efficiency and spin-polarization of the extracted beam observed at Nagoya Univ. are also given. The surfaces of the SL samples were prepared using an annealing procedure without the ion sputtering in the experimental chamber, the base pressure of which was less than 2×10^{-8} Pa. The bulk GaAs with Zn-dopants of 10^{19} cm^{-3} was also measure for comparison, the clean surface of which was prepared with Ne^{+} sputtering and annealing procedure. The NEA surface was prepared using a yo-yo technique, where cesium and oxygen were deposited repeatedly. [3]

Figure 1 shows the Ga-*3d* photoelectron spectra for the SL #1 and the SL #16 without NEA surface activation. The Ga-*3d* photoelectron spectra of the bulk GaAs are also shown for comparison. Solid and dotted lines represent the Ga-*3d* photoelectron spectra with and without the laser illumination, respectively. Under the illumination with power density of 0.17 nJ/mm^2·pulse at 90 MHz, the Ga-*3d* spectra of the SL #1 and the SL #16 shifted to higher kinetic-energy side about 0.12 and 0.03 eV, respectively. The same energy shifts of the As-*3d*

[†] present address : Research Center for Materials Science, Nagoya University, Nagoya 464-8602
[‡] present address : Synchrotron Light Application Center, Saga University, Saga 840-8502

photoelectron spectra were also observed (not shown here). These core-level shifts of the SL samples are remarkably smaller than those of the bulk GaAs under similar conditions (about 0.39 eV).

Table I. Parameters of the GaAs-GaAsP superlattices.

	SL #1	SL #16
Surface Layer	GaAs : 5 nm, 5×10^{18} cm^{-3}	GaAs : 5 nm, 6×10^{19} cm^{-3}
$GaAs\text{-}GaAs_{1-x}P_x$ Superlattice Layer	16 pairs $GaAs_{0.8}P_{0.2}$: 3 nm, 5×10^{17} cm^{-3} GaAs : 3 nm, 5×10^{17} cm^{-3}	16 pairs $GaAs_{0.64}P_{0.36}$: 4 nm, 5×10^{18} cm^{-3} GaAs : 4 nm, 5×10^{18} cm^{-3}
Optimum Wavelength (nm)	803	778
Polarization (%)	80	93
Quantum Efficiency (%)	0.3	0.6

* The dopant is Zn in all layers.

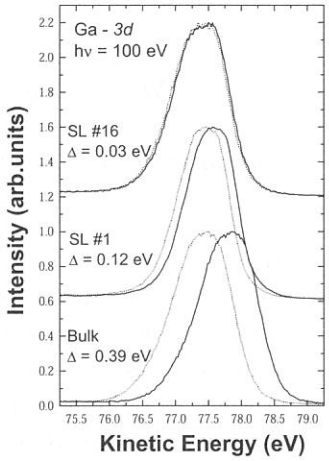

Fig. 1. The Ga-3d photoelectron spectra with (solid line) and without (dotted line) laser illumination in the non-activated surfaces. Bulk: T = 90 K. Laser; 90 MHz, 800 nm, 300 mW. SL #1 and SL #16: T = 110 K. Laser; 90 MHz, 770 nm, 300 mW.

Meanwhile, the Ga-*3d* photoelectron spectra on the NEA surface of the bulk, the SL #1, and the SL #16 were shifted about 0.35, 0.12, and 0.03 eV, respectively, under the laser illumination. It should be noted that the shift values observed under the laser illumination were not so different between with and without the NEA surface activation.

The SPV in the SLs is suppressed compared to that of bulk under the laser illumination. It is supposed that the suppression of the SPV in the SLs is dominantly due to the lifetime of photoexcited carriers shorter than that of the bulk. In the SL #1, the doping density of the surface layer is not enough to compensate the surface carrier density. Thereby the surface band-bending region probably reaches the SL structure, and thus in other words, it disturbs the formation of the mini-band between the SL layers. In this case, the energy mismatch between GaAs and GaAsP layers may work as quantum wells. Therefore, it is supposed that the transportation of photoexcited carriers is suppressed in the SL #1 and a part of carriers is trapped in the quantum well layer. The quantum well probably enhances the annihilation of photoexcited carriers, resulting in supression of the SPV. While in the SL #16, the high doping density of the surface layer is probably a dominant factor for the suppression of the SPV. The short band-bending region can promote the tunneling recombination of the photoexcited carriers. The NEA treatment would change the potential barrier and the density of the surface state. Sizable number of excited electrons can go through the surface potential barrier without trapping in the band-bending region because of the NEA property. It is therefore expected that the SPV values should be decreased in the NEA surfaces. The SPV value of the NEA surface in the SL samples was, however, not so different from that of non-activated surface. In the case of the present laser illumination with the low power density and the high repetition rate, the escaping effect of photoexcited electrons for the SPV is still unclear. Further studies are in progress to understand the dynamics of the photo-excited carriers in NEA surfaces.

References

[1] A. Herrera-Gómez *et al.*, J. Appl. Phys., **79**, 7318 (1996). [2] K. Togawa *et al.*, Nucl. Instr. and Meth. A **414**, 431 (1998). [3] S. D. Moré *et al.*, Surf. Sci. **527**, 41 (2003).

(BL7A)

The measurement of soft X-ray excited optical luminescence of a silica glass (II)

Tomoko Yoshida[1], Tetsuo Tanabe[1] and Hisao Yoshida[2]

[1]Department of Nuclear Engineering, Graduate School of Engineering, Nagoya University, Furo-cho, Chikusa-ku, Nagoya 464-8603, Japan

[2]Department of Applied Chemistry, School of Engineering, Nagoya University, Furo-cho, Chikusa-ku, Nagoya 464-8603, Japan

Introduction

Radiation effects on silica glasses are one of the main concerns for their application as optical windows, insulators and optical fibers under fusion and fission environments.(1) Although the radiation damage of silica in nuclear environments has been widely studied, the detailed damaging process and damage structure are still unknown. That is mainly because the effect of ionizing radiation, which is very important in optical materials like silica, is mixed up with the displacement effect. Recently, we have made in-situ luminescence measurements of silica glasses induced by in-reactor irradiation. This in-situ measurement was very useful for the observation of dynamic effects of ionizing radiation on the electrical property of silica (2,3) and we have applied this technique to study effects of other ionizing radiations (such as γ-ray, X-ray VUV and UV lights) on silica. In this study, we have measured the luminescence from a silica glass under the irradiation of soft X-ray near Si K-edge, and investigated the origin and the irradiation time evolution of the luminescence.

Experimental

The samples used in this work was a fused silica glass (T-1030) of 13 mm diameter and 2 mm thickness produced by Toshiba Ceramics, Japan. The measurement of luminescence of a fused silica glass induced by soft X-ray irradiation (1.8-1.9 keV) was carried out on the beam line 7A at UVSOR, Institute for Molecular Science with a stored current of 100-200 mA. The luminescence was focused by a lens in the UHV chamber to the monochromator (CP-200, JOBIN YVON) and detected by a multi-channel analyser (OMA III, EG&G PRINCETON APPLIED RESEARCH). The wavelength range (λ) from 300 to 800 nm was measured because the photon detecting efficiency in the regions of $\lambda < 300$ nm and $\lambda > 800$ nm were reduced drastically.

Results and Discussion

X-ray excited optical luminescence (XEOL)

Fig. 1 shows the observed luminescence spectra of the fused silica glass under the irradiation of soft X-rays near Si K-edge (1848 eV). An intense emission band around 400 nm was observed. Similar luminescence spectra have been measured for silica glasses under in-reactor or UV irradiation (2,3), and we have concluded that the present XEOL, 400 nm band emission, originates from an intrinsic $B_{2\beta}$ center (4) due to the electron excitation by soft X-ray. It is noteworthy that the intensity of the 400 nm emission band changed with the excitation energy of soft X-ray.

Time evolution of the intensity of XEOL

We have investigated the long term change of 400 nm XEOL intensity with the irradiation time of soft X-ray. Fig. 2 shows the results under the excitation by X-ray with the energy of 1834.8 eV (below Si K-edge) and 1858.6 eV (above Si K-edge). The intensities were normalized by the intensity at the beginning of the soft X-ray irradiation. Except the very early stage of the irradiation, the relative intensity decreased slightly with the irradiation time. Ishii et al. and Skuja (5,6) have reported that the $B_{2\beta}$ centers in silica are easily changed to E' centers by the

electron excitation under the UV laser irradiation. In addition, the transformation of $B_{2\beta}$ centers to E' centers had been found out in our separate γ-ray irradiation experiment for silica glasses (3). Therefore, we have concluded that some of the $B_{2\beta}$ centers probably changed to another types of oxygen deficiencies like E' centers by electron excitation effect, but the $B_{2\beta}$ centers were fundamentally stable against the present irradiation condition. This result may be partially due to the weak intensity of X-ray from the synchrotron in this energy region.

On the other hand, in the very early stage of the irradiation, the increase of the 400 nm band intensity is appreciable (Fig. 2(a)). The increasing rate, R, was quite different with excitation X-ray energies; R(1834.8 eV) > R(1858.6 eV). In the present stage, the origin of the initial increase and the difference of the initial increasing rate are not clear. However, such a dynamic phenomenon was observed for the first time, so far as we know, and the present results are clear indication that the in-situ observation is a powerful technique to study the dynamic radiation effects of soft X-ray on silica.

REFERENCES

[1] F.W. Clinard Jr., L.W. Hobbs, in: Physics of Radiation Effects in Crystal, Elsevier, Amsterdam, 1986, p. 442.

[2] T. Yoshida, T. Tanabe, T. Ii, T. Hara, M. Sakai and Y. Inaki, *Nucl. Instr. and Meth. B*, **2000**, 166-167, 476.

[3] T. Ii, T. Yoshida, T. Tanabe, T. Hara, M. Okada and K. Yamaguchi, *J. Nucl. Mater.* **2000**, 283-287, 898.

[4] R. Tohmon, H. Mizuno, Y. Ohki, K. Sasagane, K. Nagasawa, Y. Hama, *Phys. Rev. B*, **1989**, 55, 1337.

[5] K. Ishii, Y. Ohki, H. Nishikawa, *UVSOR Activity Report*, **1993**, 130.

[6] L. Skuja, *J. Non-Cryst. Solids*, **1998**, 239, 16.

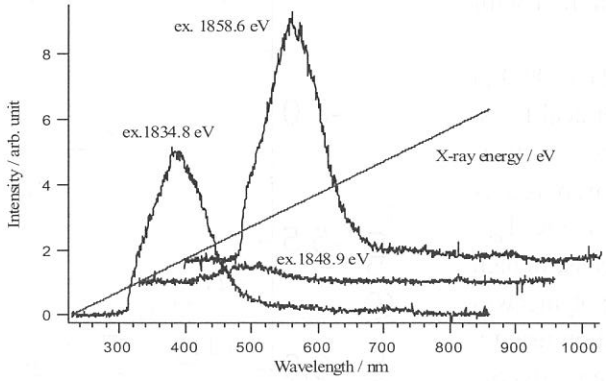

Fig.1 Optical luminescence spectra of a fused silica glass excited by soft X-ray with the energy of 1834.8 eV, 1848.9 eV and 1858.6 eV

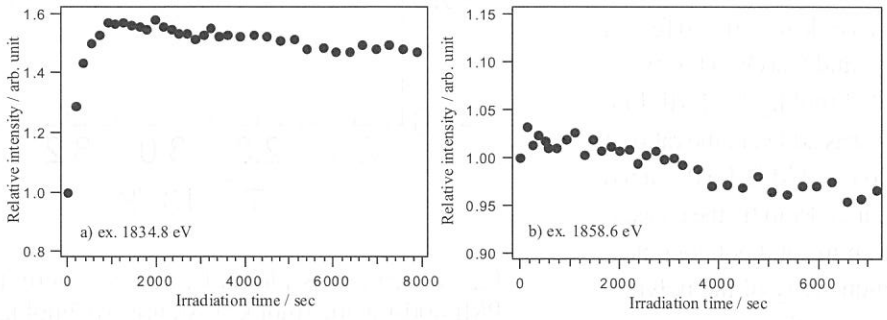

Fig. 2 The variation of the relative intensity of the band at 400 nm with the irradiation time. Excitation X-ray energies are a) 1834.8 eV and b) 1858.6 eV, respectively

(BL7A)

Preparation of novel solid polymer electrolytes containing group 13/III metal alkoxides as Lewis acid

Yoshiharu Uchimoto, Kohji Hasumi, Hiromasa Ikuta, and Masataka Wakihara

Department of Applied Chemistry, Graduate School of Science and Engineering, Tokyo Institute of Technology, 2-12-1 Ookayama, Meguro-ku, Tokyo 152-8552, Japan

There has been much interest in solid polymer electrolytes formed by the dissolution of alkali metal salts in polyethers such as poly(ethylene oxide), because of their possible application in various electrochemical devices such as lithium ion secondary batteries, sensors and displays. However, the ionic conductivity of the solid polymer electrolytes has not reached a sufficient level for practical applications. Because of the low dielectric constant of the polymer matrices, low degree of dissociation is a significant factor of the low ion conducting properties. Therefore, one approach to enhance ionic conductivity is to enhance dissociation constant of alkali metal salts in the polymer electrolytes. Recently the enhancement of the dissociation constant is achieved by adding Lewis acid which interacts with the anions. Interaction between Lewis acid and the anions is very important since it is not only to enhance of the dissociation constant but also to improve the lithium ion transference number. In this report, we have focused on group 13/III metal alkoxide having Lewis acidity as additives. The ionic conductivity of the resulting solid polymer electrolyte containing gallium triethoxide ($Ga(OC_2H_5)_3$) is one order higher than that of the electrolyte not containing alkoxides. These results indicate that Ga compounds is effective to interact with counter anions.

$Al(OC_2H_5)_3$(99.999%), $Ga(OC_2H_5)_3$(99.9%) and LiCl(99.9%up) (Kojundo Chemical Labs. Co. Ltd.) were used without further purification. $B\{(OC_2H_4)_{12}OCH_3\}_3$ was prepared as described previously.[7] $B\{(OC_2H_4)_{12}OCH_3\}_3$ was used instead of $B(OC_2H_5)_3$ because of high volatility of $B(OC_2H_5)_3$. The matrix polymer was synthesized by radical polymerization using a monomer of methoxy poly(ethylene glycol) monomethacrylate with EO chain length n=9 (abbreviated to PME400) supplied from NOF. Concentration of LiCl was fixed to 0.1 mol/kg for PME400, and two kind of different alkoxides, $Al(OC_2H_5)_3$ and $Ga(OC_2H_5)_3$ were added in the ratio of 0.2 mol/kg for PME400. $B\{(OC_2H_4)_{12}OCH_3\}_3$ was added in the ratio of 0.2 mol/kg for PME400 and $B\{(OC_2H_4)_{12}OCH_3\}_3$ in order to fix the concentration of 13 group atom in solid polymer electrolyte. The ionic conductivity of the polymer electrolyte was measured by the AC impedance techniques using Hewlett-Packard 4192A LF

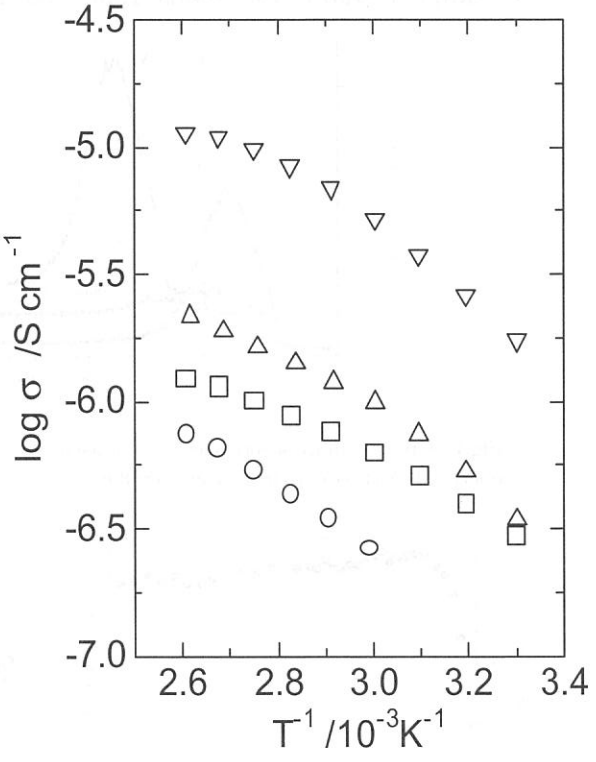

Fig. 1 Arrhenius plots of ionic conductivity for PME400-LiCl(0.1mol/kg)-Additive(0.2mol/kg). Additive for polymer electrolyte is ○ : none, △ : $B\{(OC_2H_4)_{12}OCH_3\}_3$, □ : $Al(OC_2H_5)_3$, ▽ : $Ga(OC_2H_5)_3$.

impedance analyzer. Cl *K*-edge XANES spectra were measured on the BL-7A beam line at UVSOR (Okazaki, Japan) with a ring energy of 750 MeV in a mode of total electron yield at room temperature.

The temperature dependence of ionic conductivity of the polymer electrolyte samples is shown in Fig. 1. The increase in the ionic conductivity was observed by addition of alkoxides. The degree of the increase in the ionic conductivity by added $Ga(OC_2H_5)_3$ is larger than that of any other alkoxides. The ionic conductivity of the polymer electrolyte containing $Ga(OC_2H_5)_3$ was about 10 times higher than that of none additive sample in the whole temperature range. These phenomena are generally regarded as two different factors, which are the increase in ionic mobility and the increase in carrier ion concentration. Since the glass transition temperature measured by DSC hardly changed by the addition of alkoxides, we attribute these increases in the ionic conductivity to the increase of the carrier ion concentration in the polymer electrolytes.

Interaction with Cl^- anion have been already studied using XANES experiment at the Cl *K*-edge by H. S. Lee et al.. They have reported that this technique was useful for the study of the anion complexation effects of boron-based anion receptors on Cl^- in nonaqueous solutions. Cl *K*-edge XANES is quite useful information about the local structure of the Cl^- anion. By comparing the detailed features of the XANES taken from different samples, we have investigated the anion complexation in the solid polymer electrolyte.

Fig. 2 shows the Cl *K*-edge XANES spectra of the polymer electrolyte samples. The *K*-absorption peak above the edge is due to dipole-allowed transitions to final states of p symmetry. The spectra of the polymer electrolyte samples containing $B\{(OC_2H_4)_{12}OCH_3\}_3$ or $Al(OC_2H_5)_3$ are similar to that of none additive sample, which indicates the fact that the local chemical environment around Cl^- anions is almost unchanged. The shoulder at around 2822 eV on the lower energy side of the main absorption peak was observed by the addition of $Ga(OC_2H_5)_3$. This shoulder indicates that local chemical environment around Cl^- anions partially changes, which suggests the strong interaction between Cl^- anions as Lewis base and $Ga(OC_2H_5)_3$ as Lewis acid. Since the formation of the complex between Cl^- anions and $Ga(OC_2H_5)_3$ forms new molecular orbital, the energy levels of unoccupied orbital which are allowed on the basis of dipole selection rules are lower than that of none complexing. Fig.2 indicates that $Ga(OC_2H_5)_3$ interact with Cl^- anions by XANES spectra, which results in promoting dissociation of ion pairs and improving the ionic conductivity to increase the carrier ion concentration. The solid polymer electrolytes containing group 13/III metal alkoxide having Lewis acidity showed similar electrochemical window to none additive sample. Therefore, the present polymer electrolytes are promising for a wide range of electrochemical application, such as all solid state lithium batteries.

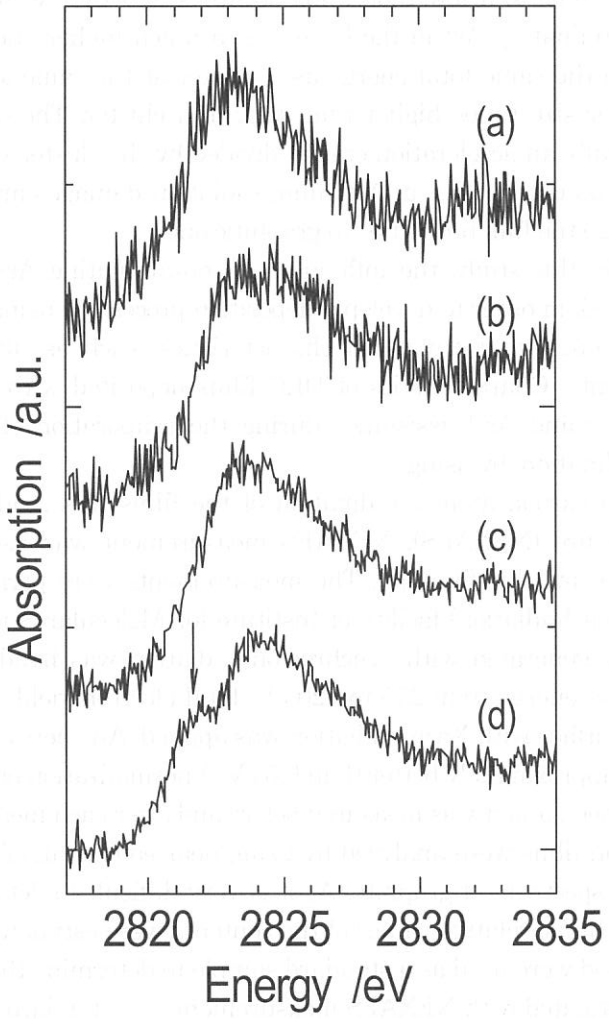

Fig. 2 Cl K-edge XANES spectra of PME400-LiCl(0.1mol/kg)-Additive(0.2mol/kg). Additive for polymer electrolyte is (a): none, (b): $B\{(OC_2H_4)_{12}OCH_3\}_3$, (c): $Al(OC_2H_5)_3$, (d): $Ga(OC_2H_5)_3$.

(BL8B1)

Effects of Ar cluster and Ar monomer ion on Diamond-Like Carbon film properties

T. Kitagawa[1,2], K. Miyauchi, K. Kanda[1,2], Y. Shimizugawa[2], N. Toyoda[2], S. Matsui[2], H. Tsubakino[1], and I. Yamada[2,3]

[1] *Himeji Institute of Technology, Faculty of Engineering, Himeji, Hyogo, Japan*
[2] *Himeji Institute of Technology, Laboratory of Advanced Science and Technology for Industry, Kamigori, Hyogo, Japan*
[3] *Collaborative Research Center for Cluster Ion Beam Process Technology, Osaka Science and Technology Center, Osaka, Japan*

In a previous study, we have demonstrated that the Gas Cluster Ion Beam (GCIB) assisted deposition was useful for forming DLC films with high hardness (~50 GPa), smooth surfaces, and low contents of sp^2 orbitals, at room temperature [1, 2]. The DLC films were formed with irradiation of an Ar cluster ion beam during evaporation of C_{60}, as a carbon source.

In our new system, Ar cluster ion beams have included various sizes of clusters in the range from a few tens to a few thousands of atoms and they were additionally supplemented by Ar^+ [2]. The contaminating Ar^+ in the beam has a much higher energy than that of a cluster. As a monomer is given the same total energy as a cluster at the same ionizer, the energy per atom of a monomer is cluster size times higher than that of a cluster. The energy of constituent atoms of the cluster is basically an acceleration energy divided by the cluster size. In the case of a diamond-based material, such as diamond or a DLC film, radiation damages are induced by energetic particles. This would change the film properties to graphitic ones.

In this study, the influences of contaminating Ar^+ in GCIB on properties of DLC films were studied, in order to develop a deposition process by using a GCIB technique; and to obtain DLC films with outstanding physical characteristics, such as ultra-hard hardness (> 50 GPa) and low sp^2 contents. Characteristics of DLC films deposited with Ar cluster ions, Ar^+, and their mixture (Ar cluster and Ar^+) assistance during the evaporation of C_{60} were studied based on a carbon atom coordination, by using.

A carbon atom coordination of the films was studied with Near Edge X-ray Absorption Fine Structure (NEXAFS). NEXAFS measurement was useful to obtain information of sp^2-hybridized orbital in DLC films [3]. The measurements were performed at UVSOR (Ultra-Violet Synchrotron Orbital Radiation) facility of Institute for Molecular Science using the beam-line 8B1 in Japan. Soft X-ray generated with synchrotron radiation was irradiated to the film at normal incidence, with photon energy from 275 to 320 eV. Total electron yield mode that counted all electrons emitted from the surface with X-ray radiation was applied. An energy resolution of a monochromator with a grating was approximately better than 0.5 eV. A normalization of spectra was performed with the spectra of an Au sheet, and it was measured before and after each measurement of carbon films. The sp^2 contents in carbon films were analyzed by using near edge peak of π^* resonance (285.5 eV), which was referred from spectrum of graphite. As it is very difficult to determine absolute values of sp^2 contents of the DLC films, relative values of the contents were estimated. The DLC films deposited with RF plasma method were used as a standard sample to determine those values. Additionally, the C_{60} film was also investigated with NEXAFS measurement as a standard carbon film.

Figure 1 shows NEXAFS spectra of carbon films formed by various ion beam assisted depositions. The C_{60} film and the RF plasma DLC film are also presented in figure 1. The NEXAFS spectrum of C_{60} film showed three π^* peak of the carbon K edge (284.5eV, 285.5 eV, and 287.4 eV). This result showed a good agreement with the previous theoretical study [4]. These sharp peaks became smaller or disappeared in the spectra of the films irradiated with various Ar ion beams, except for a peak of

285.3 eV. This means that C_{60} molecules were broken by irradiation of various Ar ion beams and the films were changed to amorphous ones. The spectrum of the films formed with Ar^+ irradiation had a small peak at 287eV, which was the same position as the third peak of C_{60}. Additionally a σ^* broad peak around 294 eV was also similar to that of C_{60}. Thus structures of C_{60} were still remained in the film formed by Ar^+ assisted deposition. On the other hand, the films irradiated with Ar cluster ions and the mixture had no structure of C_{60}. However, a slightly lager peak at 285.3 eV was obtained from the film with the mixture irradiation. This peak at 285.3 eV was originated from *sp* and sp^2 hybridized orbital of carbon bonding [3]. The peak is usually considered as sp^2 orbital because the *sp* orbital is not stable. Integral of this peak in the spectra that is useful to discuss sp^2 contents in films was shown in table 1. The integrals of the peaks were normalized with that of RF plasma DLC as a reference. The smallest integral of the peak was obtained from the films by cluster ion beam assisted deposition. With increasing Ar cluster ion in the beam, the integral of the peak decreased. Therefore, it indicated that when fraction of Ar^+ was higher, sp^2 contents also became larger due to graphitization of carbon.

Acknowledgements

The authors would like to appreciate Dr. Tatsuo Gejo and Dr. Eiken Nakamura for operation of the beam line at UVSOR. This work is supported by New Energy and Industrial Technology Development Organization (NEDO) and the Joint Studies Program of the Institute for Molecular Science.

[1] T. Kitagawa, I. Yamada, N. Toyoda, H. Tsubakino, J. Matsuo, G.H. Takaoka, and Allen Kirkpatrick, Nucl. Instr. and Meth. in Phys. Res. B, submitted.

[2] K. Kanda, T. Kitagawa, Y. Shimizugawa, Y. Haruyama, S. Matsui, M. Terasawa, H. Tsubakino, I. Yamada, T. Gejo, and M. Kamada, Jpn. J. Appl. Phys., 41, 4295, (2002).

[3] C.Lenardi, P. Piseri, V. Briois, C.E. Bottani, A. Li BassiP. Milani, J. Appl. Phys., **85**, 7159, (1999).

[4] L.J.Terminello, D.K. Shuh, F.J.Himpsel, D.A. Lapiano-Smith, J.Stohr, D.S. Bethune and G. Meijer, Chem. Phys. Lett., **82**, 491, (1991).

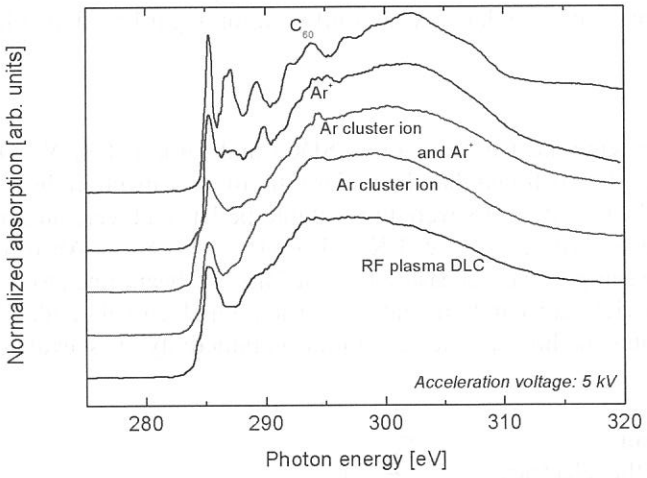

Figure 1. NEXAFS spectra of carbon films formed with various Ar ion beam assisted depositions. The C_{60} film and DLC film formed by RF plasma method were mesured to obtain standard spectra.

TABLE I. INTEGRALS OF π^* PEAK (285.3 EV) EXTRACTED FROM NEXAFS SPECTRA OF THE FILMS IRRADIATED WITH VARIOUS ION BEAM IRRADIATIONS. THE PEAK INTEGRALS WERE NORMALIZED WITH THAT OF THE FILMS BY RF PLASMA METHOD AS A STANDARD.

Incident Ion species	Ar cluster ion	Ar cluster and Ar^+	Ar^+
Integral of π^* peak	0.68	0.99	1.18

(BL8B1)

Electronic Structure of $Ce_{0.8}M_{0.2}O_{2-\delta}$ (M; Sm and Y) Evaluated from O K-edge XANES

Atsushi Mineshige[A], Noriyuki Ohmura[A], Masafumi Kobune[A], Tetsuo Yazawa[A] and Yoshiharu Uchimoto[B]

[A]*Department of Applied Chemistry, Graduate School of Engineering Himeji Institute of Technology*
Shosha 2167, Himeji, Hyogo 671-2201, Japan
[B]*Department of Applied Chemistry, Graduate School of Science and Engineering, Tokyo Institute of Technology*
Ookayama, Meguro, Tokyo 152-8552, Japan

1. Introduction

Doped CeO_2 (ceria) is one of the successful candidates for electrolyte materials of solid oxide fuel cells (SOFCs) because of its high oxide ion (O^{2-}) conductivity, and has been widely investigated so far [1]. Electrolyte materials in SOFCs are placed between air and fuel (*i.e.* under influence of large $P(O_2)$ gradient at elevated temperatures. Since doped ceria has considerable n-type electronic conductivity as well as oxide ion conductivity under reducing conditions, as is encountered in the fuel-side of SOFCs, it is important to suppress its electronic conduction for development of high performance ceria-based SOFCs. In addition, it was recently reported that the system has p-type electronic conductivity as well [2].

The appearance of n-type electronic conduction at the low $P(O_2)$ region is due to partial reduction of Ce^{4+} into Ce^{3+} by the reducing power of the surrounding gases. The authors have already developed the novel method to determine concentration of Ce^{3+} in oxides using Raman spectroscopy [3]. The aim of this work is to evaluate localized position and concentration of p-type charge carriers in doped CeO_2 to know details in its electronic conducting behavior. In the previous report [4], the electronic structure of p-type semiconductor, (La, Sr)(Co, Fe)O_3, was studied using the same beam line by measuring XANES spectra at Co L_{23}-edge, Fe L_{23}-edge and O K-edge. In the present study, O K-edge XANES spectra of doped ceria were measured in a similar way, and information regarding doped hole states at oxygen sites was obtained.

2. Experimental

Doped ceria with samaria, $Ce_{0.8}Sm_{0.2}O_{2-\delta}$ (SDC) and yttoria, $Ce_{0.8}Y_{0.2}O_{2-\delta}$ (YDC) was prepared from each metal nitrate. It was found that the molar ratio of each metal in the powders thus obtained was desirable by an ICP analysis. Powders were pressed into pellets and were annealed under atmospheres of pure oxygen, air or diluted hydrogen at 1273 K. The O K-edge X-ray Absorption Near Edge Structure (XANES) spectra of the samples were measured on the BL-8B1 beam line at UVSOR (Okazaki, Japan) in a mode of total electron yield at room temperature. The total electrical conductivity was measured using conventional d.c. 4-probe method and its electronic conductivity was evaluated by the ion blocking method.

3. Results and discussion

Figure 1 shows the electrical conductivity (σ) of YDC at 1073 and 1273 K in the range $10^{-8} \leq [P(O_2)/\text{atm}] \leq 1$. The ionic conductivity was shown as a dashed line in this figure assuming that it can be regarded as $P(O_2)$ independent and equal to the total conductivity under air. The electronic conductivity determined by the ion blocking method was plotted against $P(O_2)$ as symbols. Though the data show some scatter, they are clearly in proportion to $P(O_2)^{\pm 1/4}$. The p-type

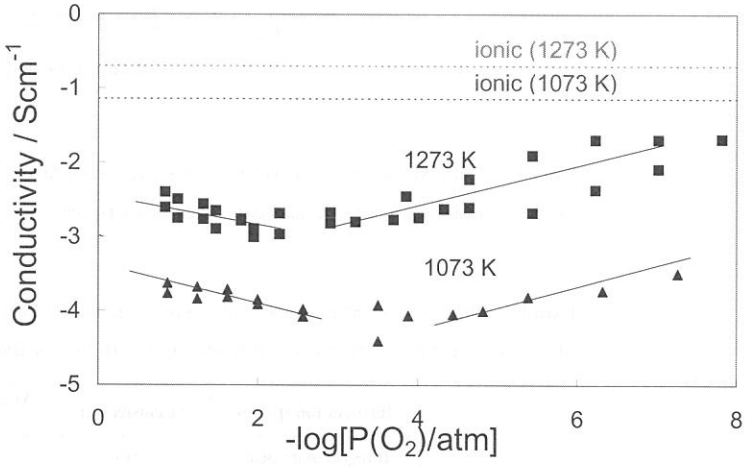

Fig. 1. Electronic conductivity of $Ce_{0.8}Y_{0.2}O_{2-\delta}$ as a function of $P(O_2)$.

electronic conduction became predominant in the range $P(O_2) \geq 10^{-2}$ atm at 1273 K.

Figure 2 shows O *K*-edge XANES of $Ce_{0.8}Y_{0.2}O_{2-\delta}$ after annealing and quenching in various atmospheres. While the hydrogen-annealing sample had similar XANES spectrum to that of the sample fired in air, the peak edge of the oxygen-annealing sample shifted to lower energy. This may be because the hole state, containing O 2*p* character was doped by high $P(O_2)$ annealing. In the previous report on the electronic structure of (La, Sr)(Co, Fe)O_3, the prepeak was observed in its O *K*-edge XANES which is attributed to the doped hole state, and it disappeared along with the oxygen vacancy formation with decrease in $P(O_2)$. Hence it was concluded that oxygen atoms containing this hole state with O 2*p* character may be transformed easily into neutral oxygen molecules under low $P(O_2)$, leaving the oxygen vacancies at the lattice. In the case of doped ceria, exhibiting oxygen nonstoichiometry as well, it was suggested that the hole state with O *2p* character also pay an important role against oxygen introduction and evolution. With $P(O_2)$ increases, doped ceria undergoes *n* to *p* transition as shown in Fig. 1, whereas it is not observed for (La, Sr)(Co, Fe)O_3 system. In the *n*-type region [$P(O_2) \leq$ ca. 10^{-2} atm], oxygen reduction and incorporation on the sample surface is accompanied by oxidation of Ce^{3+} to Ce^{4+} *i.e.* decrease in *n*-type carriers. Since there were no significant differences of XANES spectra between hydrogen-annealed and air-fired samples, electron hole states at the O *2p* site are almost empty. Beyond the critical $P(O_2)$, ca. 10^{-2} atm at 1273 K, reductant such as Ce^{3+} has been almost consumed and the system gets into the *p*-type region. In the *p*-type region, it is hard to reduce oxygen ($O_2 \rightarrow O^{2-}$) for lack of donor electrons from the reductant. Hence oxygen with doped hole is incorporated into the lattice. This is the origin of *p*-type electronic conduction of doped ceria.

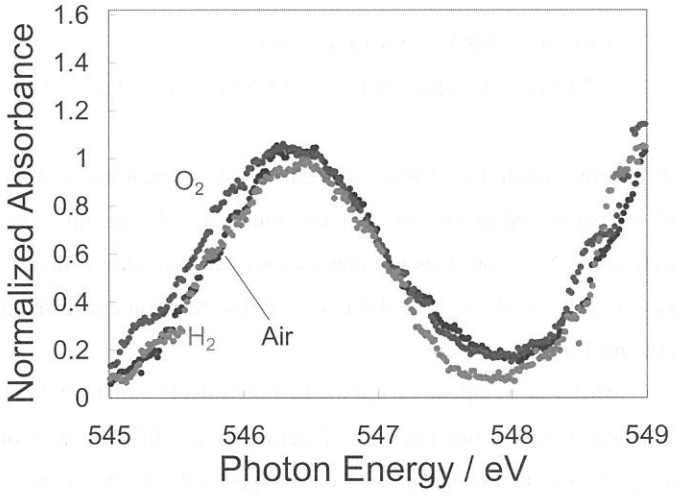

Fig. 2. O1s X-ray absorption spectra of $Ce_{0.8}Y_{0.2}O_{2-\delta}$.

Figure 3 shows the O *K*-edge XANES of SDC. While similar behavior was observed, the hole concentration of oxygen-annealing sample looks larger than the YDC case. The reason is not clear at present. In the further work, a quantitative observation regarding the hole concentration and study on dependency of dopants should be done.

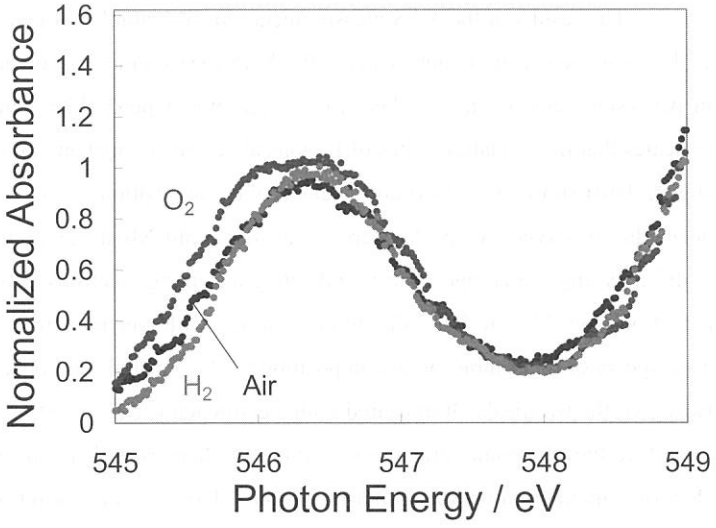

Fig. 3. O1s X-ray absorption spectra of $Ce_{0.8}Sm_{0.2}O_{2-\delta}$.

References

[1] K. Eguchi, T. Setoguchi, T. Inoue and H. Arai, *Solid State Ionics*, **52**, 165 (1992).

[2] Y. Xiong, K. Yamaji, N. Sakai, H. Negishi, T. Horita, and H. Yokokawa, *J. Electrochem. Soc.*, **148,** E489 (2001).

[3] A. Mineshige, T. Taji, Y. Muroi, M. Kobune, S. Fujii, N. Nishi, M. Inaba and Z. Ogumi, *Solid State Ionics*, **135**, 481 (2000).

[4] A. Mineshige, M. Kobune, S. Fujii and Y. Uchimoto, *UVSOR Activity Reort.2002,* **UVSOR-29,** 200 (2002).

(BL-8B1)

Changes in electronic structure accompanying lithium insertion into the perovskite type oxides using X-ray absorption spectroscopy measurement

Yoshiharu UCHIMOTO, Masanobu NAKAYAMA, Masataka WAKIHARA

Dept. of Appl. Chem., Tokyo Institute of Technology, Ookayama, Meguro-ku, Tokyo 152-8552, Japan.

Transition-metal oxides having lithium insertion sites are particularly interesting as the electrode material of lithium ion batteries with high-energy density. And these materials are attractive also for the good examples of the basic study of solid-state electrochemical reaction, since the host crystal structure is almost same before and after electrochemical reaction. A-site deficient perovskite type oxide, $La_{1/3}NbO_3$, is considered to be a candidate for these model compounds [1]. In addition, it is known that there are two types of lithium insertion reaction in this perovskite type compound, one is electrochemical Li^+ insertion reaction (eq.1) and the other thermal Li+ insertion reaction (eq.2), respectively. (The latter is expressed more accurately as the substitution of Li^+ for La^{3+} in perovskite A-site.)

$$x\ Li + La_{1/3}NbO_3 \rightarrow Li_xLa_{1/3}NbO_3 \qquad (1)$$

$$y/2\ Li_2O + (1\text{-}y)\ La_{1/3}NbO_3 + y/2\ Nb_2O_5 \rightarrow Li_yLa_{(1-y)/3}NbO_3 \qquad (2)$$

The reaction shown in eq.1 is classified as a redox reaction, and it is considered in conventional chemical sense that the Nb^{5+} ion is reduced to Nb^{4+} ion. On the other hand, the reaction described in eq.2 does not accompany a redox reaction, therefore the Nb^{5+} ion does not change its oxidation state. In this study [2], we investigate the variation of oxidation states of each ion through the lithium insertion reaction expressed as eq.1 and eq.2 by x-ray absorption spectroscopy (XAS) measurement.

Different compositions of the $Li_yLa_{(1-y)/3}NbO_3$ solid solution were prepared by conventional solid state reaction. The details were described in ref 1. Electrochemical lithium insertion was carried out by galvanostatic method (current density; 40mA/cm^2) using three-electrode type cell. The XAS measurements for the La L_{III}-edge spectra were carried out by transmission mode. And that of Nb L_{III}-edge and O K-edge spectra were carried out by total-electron-yield method. For the samples after electrochemical treatment, all installation operations were performed under Ar or N_2 atomosphere.

The results of the XAS measurements for the samples of electrochemical lithium insertion are shown in figure 1. La L_{III}-edge spectra (figure 1(a)) of the XAS measurements show no marked change, and formal charges of La ions in perovskite samples are +3 because the spectra of perovskite samples were consistent with that of La_2O_3. This indicates that the oxidation states of La ions at A-site are unchanged throughout the reaction. The Nb L_{III}-edge spectra (figure 1(b)) show two absorption peaks at the composition x = 0. Concerning the crystal field theory for the NbO_6 octahedra, observed two peaks were assigned as split Nb4d, t2g and eg orbital. The intensity of t_{2g} peak decreased with increasing the composition x, indicating accepting electrons into t_{2g} orbital by reduction reaction. Therefore the reduction from Nb^{5+} to Nb^{4+} should occur along with electrochemical lithium insertion. Figure 1(c) shows the O K-edge specra of the samples with composition x. Two peaks were observed at x = 0 in the range from 525eV to 535eV. However, the two peaks disappeared with electrochemical Li insertion, and an additional peak appeared at about 532eV. Therefore the electronic structure of oxide ion changes with Li insertion reaction and maybe due to the changes in electronic interaction with neighboring cations. There are three kinds of cations interacting with oxide ion, Nb, La and Li , respectively. The interaction between La and O should not affect the changes in electronic structure of oxide ions due to no marked change in XAS spectra (Fig.1a). Hence, the changes in electronic structure of oxide ions will be explained by two hypotheses. (i) due to the changes in the interaction of Nb-O, and/or (ii) the increment of Li-O interaction with increasing the amount *x*. In order to clarify the reason for the variation of O K-edge spectra, we

investigated the XAS spectra of thermally Li^+ inserted samples. The results of Nb L_{III}-edge did not alter with composition y, indicating Nb ions keep their formal oxidation state as +5 through the lithium insertion as expected equation.2 (Figure 2). On the other hand, the O K-edge spectra vary with thermal Li^+ insertion and are similar to the spectra for the samples with electrochemical Li^+ insertion (Figure 2). Accordingly the origin of variation of electronic structure of oxide ions is due to the interaction between lithium ion and oxide ion, or the variation of ionicity of oxide ions.

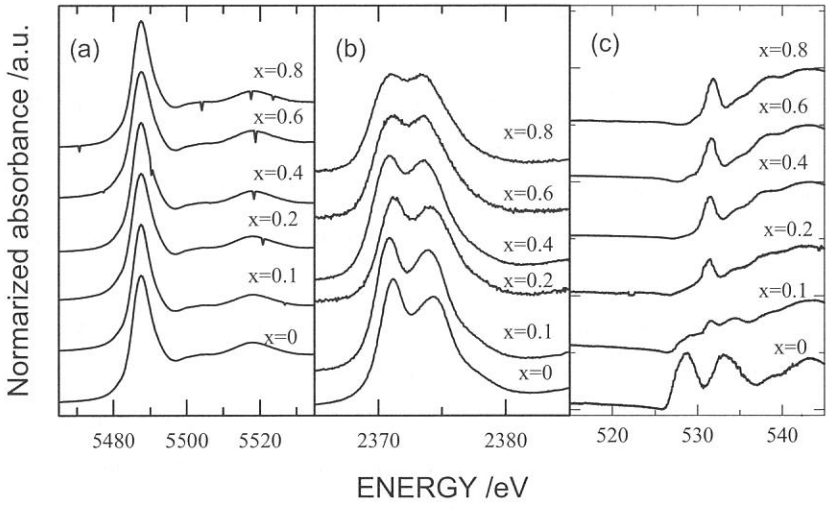

Figure 1. The variation of XAS spectra with electrochemical lithium insertion for the samples, $Li_xLa_{1/3}NbO_3$. (a):La L_{III}-edge, (b):Nb L_{III}-edge, (c):O K-edge. (x=0, 0.1, 0.2, 0.4, 0.6, 0.8)

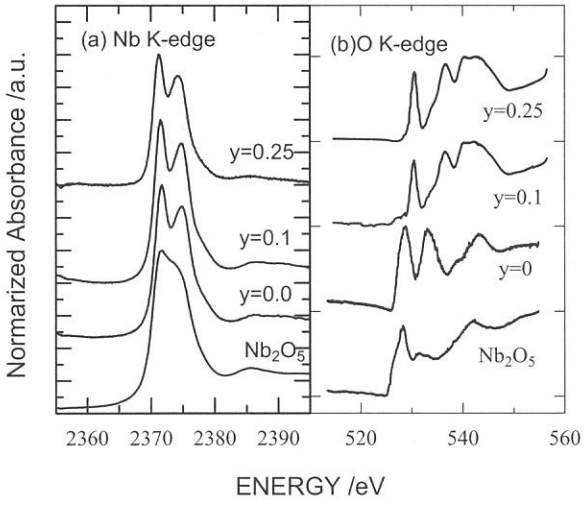

Figure 2. The variation of XAS spectra with thermal lithium insertion for the samples, $Li_yLa_{(1-y)/3}NbO_3$. (a)::Nb L_{III}-edge, (b):O K-edge. (x=0, 0.1, 0.25)

REFERENCE

1. M.Nakayama et al., J. Phys. Chem. B. 106, 25, 6437, (2002).
2. M. Nakayama et al., Chem. Mater., (2003), in press.

(BL-8B1)

Charge Compensation in CoV_3O_8 Accompanied by Li Insertion Analyzed from Co-*L* and V-*L* XANES

Naoshi OZAWA, Takashi MURAKAMI and Takeshi YAO

Graduate School of Energy Science, Kyoto University, Kyoto, 606-8501 Japan

Novel cobalt vanadium oxide CoV_3O_8 crystallizes in orthorhombic system *Ibam* and has tunnel-like space along c-axis in the crystal structure. [1] It is considered that the tunnel-like space is advantageous for lithium ion insertion and deinsertion. In the present study, we have synthesized CoV_3O_8 and inserted Li into the CoV_3O_8 electrochemically. The charge compensation in CoV_3O_8 accompanied by the Li insertion was analyzed from Co-*L* and V-*L* XANES.

CoV_3O_8 was synthesized by solid-state reaction. Electrochemical lithium insertion was carried out by using a three-electrode cell. The working electrode consisted of 80 mass% of active material, 15 mass% of acetylene black powder and 5 mass % of a binder (polytetrafluoro ethylene). The counter and reference electrode were lithium metal. The electrolyte was 1 mol·dm^{-3} $LiClO_4$ dissolved in propylene carbonate. Lithium was inserted into CoV_3O_8 at constant current density of 0.5 mA·cm^{-2} and $Li_xCoV_3O_8$(x=0, 0.7, 1.3, 2.6) were obtained. X-ray absorption was measured by BL-8B1 at UVSOR, Institute for Molecular Science, Okazaki, Japan. The storage ring was operating at electron energy of 750 MeV. The spectra were collected in a total electron yield mode at room temperature by an electron multiplier using G1 diffraction grating.

Figure 1 shows Co-*L* XANES for $Li_xCoV_3O_8$(x=0, 0.7, 1.3, 2.6). Co-*L* XANES for CoO (Co^{2+}) and $LiCoO_2$ (Co^{3+}) were also given as references. It can be seen from Fig. 1 that the valence of Co in $Li_xCoV_3O_8$(x=0, 0.7, 1.3, 2.6) would be +2. This indicates that valence of Co was unchanged during Li^+ ion insertion into CoV_3O_8. Figure 2 shows V-*L* XANES for $Li_xCoV_3O_8$(x=0, 0.7, 1.3, 2.6). V-*L* XANES for V_2O_3 (V^{3+}), V_2O_4 (V^{4+}), V_2O_5 (V^{5+}) were also given as references. The profile of V-*L* edge of CoV_3O_8 resembles those for V_2O_4 and V_2O_5. This indicates that the valence of V in CoV_3O_8 would be +4 or +5. The value is compatible with average valence of V in CoV_3O_8, +4.67, which is calculated by assuming that valence of Co is +2. Shifts of L_{III} peak at ~520 eV and L_{II} peak at ~528 eV to lower energy with increase of Li content x was observed and the profile of $Li_{2.6}CoV_3O_8$ became similar to that for V_2O_3. This result indicates that V in CoV_3O_8 was reduced by the electrochemical Li^+ ion insertion.

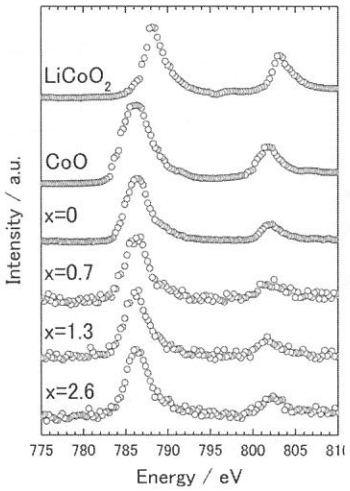

Fig. 1 Co-*L* XANES for $Li_xCoV_3O_8$(x=0, 0.7, 1.3, 2.6). Co-*L* XANES for CoO (Co^{2+}) and $LiCoO_2$(Co^{3+}) were also given as references.

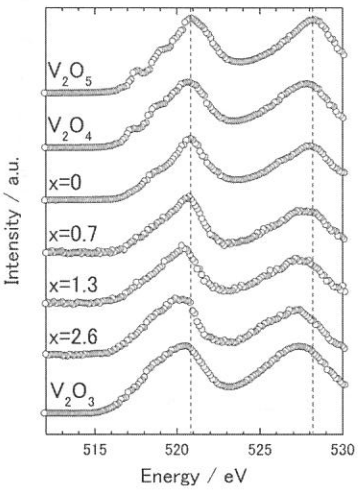

Fig. 2 V-*L* XANES for $Li_xCoV_3O_8$(x=0, 0.7, 1.3, 2.6). V-*L* XANES for V_2O_3(V^{3+}), V_2O_4(V^{4+}), V_2O_5(V^{5+}) were also given as references.

[1] Y. Oka, T. Yao, N. Yamamoto and Y. Ueda, *J. Solid State Chem.*, **141**, 133-139(1998).

(BL8B2)

Resonant Photoemission Study of $Li_xNi_{2-x}O_2$ using Synchrotron Radiation

T. Miyazaki[a], D. Yoshimura[b], K. Okudaira[b] and T. Yamaguchi[a]

[a]*Department of Applied Chemistry, Faculty of Engineering, Ehime University, Matsuyama 790-8577, Japan*

[b]*Institute for Molecular Science, Myodaiji, Okazaki 444-8585, Japan*

A layered structure $LiNiO_2$, which can be thought of as an ordered rock-salt type with an ABCABC stacking of oxygen planes and Li and Ni ions ordered in alternate octahedral sites of (111) planes, is one of the most studied cathode materials for the application in the lithium ion batteries. The lattice oxygen species of $Li_xNi_{2-x}O_2$ ($x>0.6$) with a layered structure has also a selectively catalytic property for an oxidative coupling of methane, while those of $Li_xNi_{2-x}O_2$ ($x\leqq0.6$) with a non-layered structure completely oxidize methane to the carbon dioxide. The top of the valence band region usually determines the chemical properties of the materials; therefore, it should be carefully investigated. Then, the electronic structure of $Li_xNi_{2-x}O_2$ ($0<x\leqq1$) was examined from the incident photon energy dependence of UPS (Ultraviolet photoelectron spectra) in order to clarify the origin of selective catalysis and electronic structures.

The solid solution series $Li_xNi_{2-x}O_2$ ($0<x\leqq1$) were prepared from $LiNO_3$ and $Ni(OH)_2$ by solid-state reaction. The ultraviolet photoelectron spectra were measured using solid photoelectron spectroscopy equipment (BL8B2). The surface treatment of samples was scraped by a diamond file in a chamber kept around 10^{-9} Torr and was done to Ar^+ sputtering.

Fig. 1 compares the UPS of $Li_{0.1}Ni_{1.9}O_2$, $Li_{0.3}Ni_{1.7}O_2$, $Li_{0.5}Ni_{1.5}O_2$, $Li_{0.8}Ni_{1.2}O_2$ and $LiNiO_2$ at 40eV incident photon energy. These spectra were measured with reference to E_F as the zero of the energy scale. The photoionization threshold of $Li_xNi_{2-x}O_2$ is evaluated from the UPS spectral onset to be 0.4～1.2eV relative to E_F, respectively. The top of the valence band of $Li_xNi_{2-x}O_2$ is derived from Ni and O. These spectra are mainly five features, and can be attributed to Ni3d (A, 1.6～2.5eV), unknown (B, 3.2～3.9eV), $O2p_z$ (C, 5.0～6.0eV), $O2p_{xy}$ (D, 6.8～7.5eV) and Ni3d satellite (E, 9.7～11.5eV). The photoemission intensity of $LiNiO_2$ is dependent on the incident photon energy as shown in Fig. 2. The Ni3p→Ni3d core absorption edge is located at around 65eV, and the intensity of peak A and D changes resonantly at the absorption edge. Comparing the electronic structures of $Li_xNi_{2-x}O_2$ ($x\leqq0.6$) and $Li_xNi_{2-x}O_2$ ($x>0.6$), several differences are found. In $Li_{0.1}Ni_{1.9}O_2$, $Li_{0.3}Ni_{1.7}O_2$ and $Li_{0.5}Ni_{1.5}O_2$, there exists a considerable possibility of orbital mixing between Ni and O, although there is no such evidence in $Li_{0.8}Ni_{1.2}O_2$ and $LiNiO_2$. It is evident that these differences affect the catalytic selective oxidation for the OCM reaction.

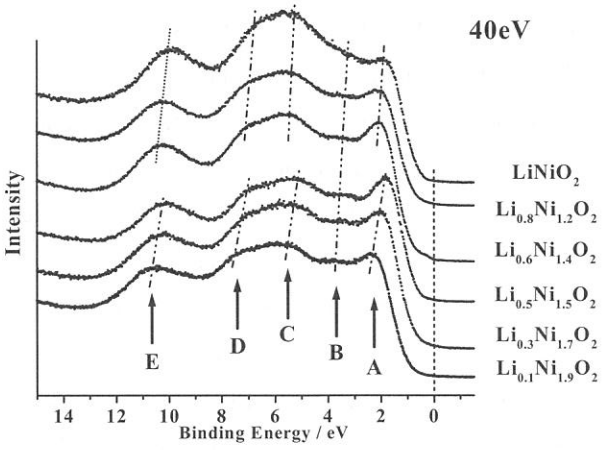

Fig.1. The UPS of $Li_xNi_{2-x}O_2$ ($0<x\leqq1.0$).

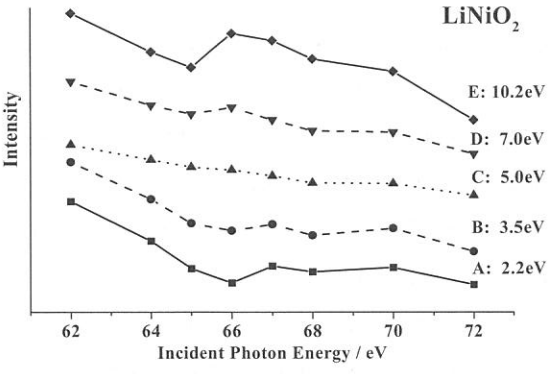

Fig. 2. The *hν* dependence of the UPS of $LiNiO_2$.

(BL8B2)

Two-dimensional film structure and electronic structure of NTCDA single-domain monolayer by angle-resolved UPS

Satoshi KERA[a], Hiroyuki YAMANE[a,b], Shinji TANAKA[a],
Daisuke YOSHIMURA[b,c], Koji K. OKUDAIRA[b], Kazuhiko SEKI[c] and Nobuo UENO[a]

[a]*Graduated School of Science and Technology, Chiba University, Chiba 263-8522*

[b]*Institute for Molecular Science, Okazaki 444-8585*

[c]*Research Center for Materials Science, Nagoya University, Furo-cho, Chikusa-ku, Nagoya 464-8602*

Origins of the energy position and the width of HOMO bands are keys to understand interface properties, such as the energy level alignment and molecule-molecule and/or molecule-substrate interaction in organic devices. The angle-resolved UPS using synchrotron radiation is a powerful tool to study the geometrical structure of the ultrathin films of organic molecules as well as the electronic structure. In the previous work we analyzed the take-off (θ) and azimuthal (ϕ) angle dependencies of ARUPS of thin films of large organic molecules using independent-atomic-center and single-scattering approximations combined with molecular orbital calculation (IAC/MO and SS/MO). We succeeded to determine quantitatively the molecular arrangement and orientation of Cu-, ClAl-phthalocyanine/MoS_2 [1], BTQBT/MoS_2 [2], and PTCDA/MoS_2 [3] etc. However, it is difficult to understand precise electronic state for these organic molecules on the MoS_2 substrate due to the existence of multi-domains. An organic single-domain monolayer can be an excellent model in studying what is happening just at organic-inorganic interface by using UPS.

Recently, in the monolayer, we found that naphthalene-1,4,5,8-tetracarboxylic dianhydride (NTCDA) molecules were oriented with their molecular plane flat to the substrate, and showed the single-domain film could be formed on a GeS(001) substrate surface by means of LEED. In the present work, we report results of quantitative analysis of the θ and ϕ dependencies of the photoelectron intensity from the valence bands by comparison between ARUP spectra and SS/MO calculations for the NTCDA monolayer deposited on the GeS substrate.

ARUPS measurements were carried out at the BL8B2 of UVSOR. ARUP spectra were measured by a newly installed system of a VG-ARUPS10 analyzer with a multi channel detector system. The θ and ϕ dependencies were measured at photon incidence angle α = 50° and at hv = 60eV. A GeS (001) single crystal was cleaved in the UHV. A purified NTCDA

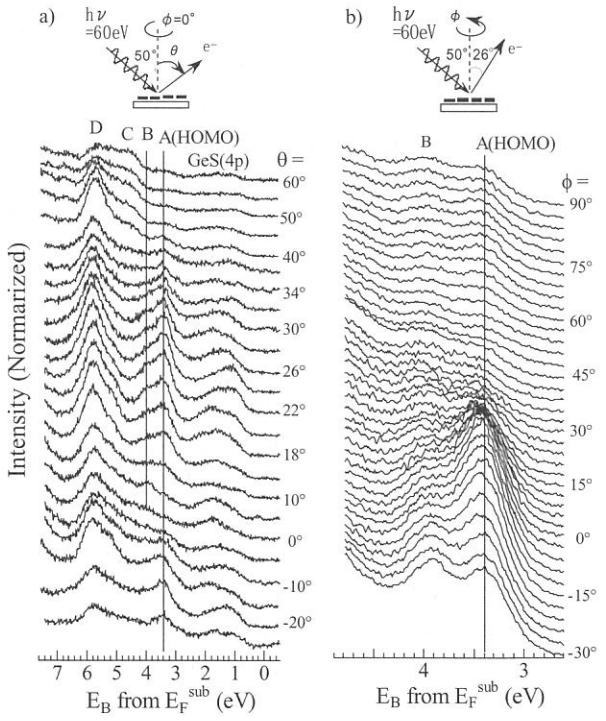

Fig.1 a) θ- and b) ϕ- dependencies of ARUPS of NTCDA (2.5Å) on GeS(001) at room temperature

was carefully evaporated onto the GeS surface. The film thickness and the deposition rate (~ 1.2 Å/min.) were measured with a quartz microbalance.

The single-domain NTCDA film exhibited a clear LEED pattern. From the analysis of the diffraction pattern, the formation of single-domain structure was confirmed. It has the rectangular unit cell with the dimensions of 9.8 Å ($2.7a_1$), 17.2 Å ($4a_2$).

Figure 1 shows the θ- and ϕ-dependencies of the ARUPS of NTCDA (2.5Å) on GeS at room temperature. Angle dependencies of photoelectron intensities are clearly seen.

Figure 2 shows the θ dependence of the photoelectron intensity from the HOMO band (single π-MO) and the calculated results for the molecular tilt angle of β = 0° and 10° using the SS/MO(HF/STO-6G) method. Among these, the calculated θ pattern for β = 0° gave the best agreement with the observed one. It indicates that NTCDA molecules orient flat to the substrate surface. Results of the ARUPS simulation using SS/MO calculation also showed a good correspondence to the overall spectral features.

Figure 3 shows the comparison between the observed and calculated ϕ dependencies of the HOMO-band intensities for the flat-lie molecular orientation. In this calculation, we averaged ϕ patterns corresponding to two different azimuthal orientations due to glide-reflection symmetry of NTCDA unit cell, which were determined by LEED. From these results, the two-dimensional NTCDA single-domain structure on GeS (001) single crystal was determined as shown in Fig.4.

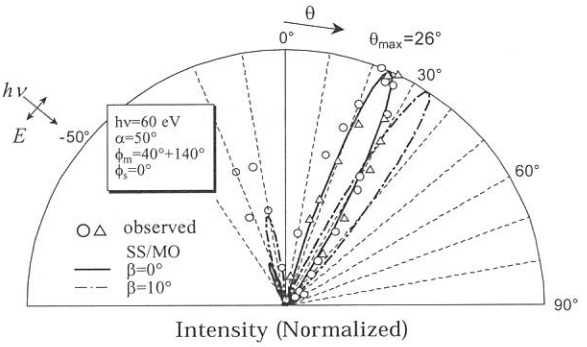

Fig.2 The comparison between calculated (-) and observed (○,△) θ-dependencies of the photoelectron intensity of the HOMO band.

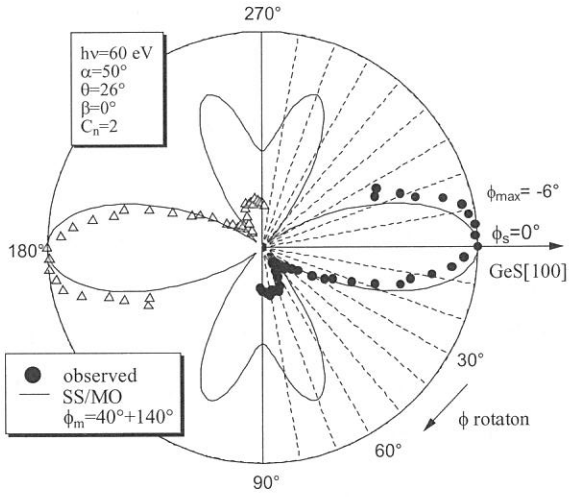

Fig.3 The comparison between calculated (-) and observed (●original range, △180° shifted) ϕ-dependencies of the photoelectron intensity of the HOMO band.

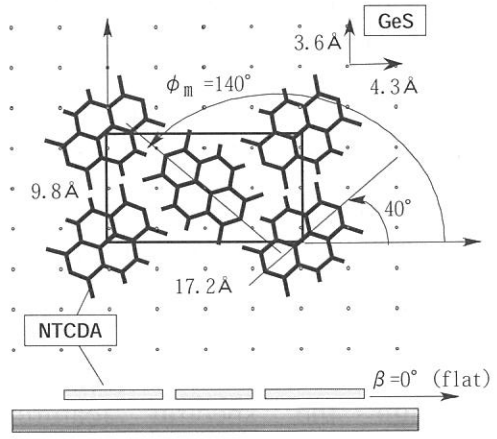

Fig.4 Two dimensional structure of NTCDA single-domain film on GeS(001) determined by ARUPS and LEED.

References

[1] K. Kamiya et al., J. Erectron Spectrosc. Relat. Phenom. **76**, 213 (1995).

[2] N. Ueno et al., J. Chem. Phys. **107**, 2079 (1997).

[3] Y. Azuma et al., J. Synchrotron Rad. **5**, 1044 (1998).

(BL8B2)

Electronic Structure of F_{16}-Zn Phthalocyanine Thin Film

Kaname KANAI[1], Takahiro YOKOYAMA[1], Tadanobu IKAME[1], Daisuke YOSHIMURA[2] and Kazuhiko SEKI[2]

[1] *Department of Chemistry, Graduate School of Science, Nagoya University, Nagoya 464-8602, Japan*

[2] *Research Center for Materials Science, Nagoya University, Nagoya 464-8602, Japan*

Metal phthalocyanines have been extensively studied in relation to a wide range of the applications utilizing their thermal and chemical stability. Recently their fluorinated derivatives also attract attention, since the electron acceptor nature of phthalocyanines can be enhanced and controlled by fluorine substitution. Such aspect is useful for constructing various organic electronic devices. Thus it is interesting to study the effect of fluorination on the electronic structure.

In this work, we studied the electronic structures of zinc phthalocyanine (ZnPc) and its perfluorinated derivative with 16 fluorine atoms (F_{16}-ZnPc) by ultraviolet photoelectron spectroscopy (UPS) using synchrotron radiation. The experiments were performed at beamline 8B2 of UVSOR facility. The samples were prepared by vacuum evaporation on a Au substrate.

In Fig. 1, we show the observed valence band spectrum of ZnPc at photon energies of 40 eV. Also we show the spectrum taken with a conventional HeI discharge ($h\nu$ = 21.2 eV) and the density of states of ZnPc calculated by GSCF3 method [1,2] as the shadow at the bottom of the figure. The correspondence is fairly good, and we can assign the spectral features corresponding to the π and σ(C-C) states in the observed spectra as indicated in the figure.

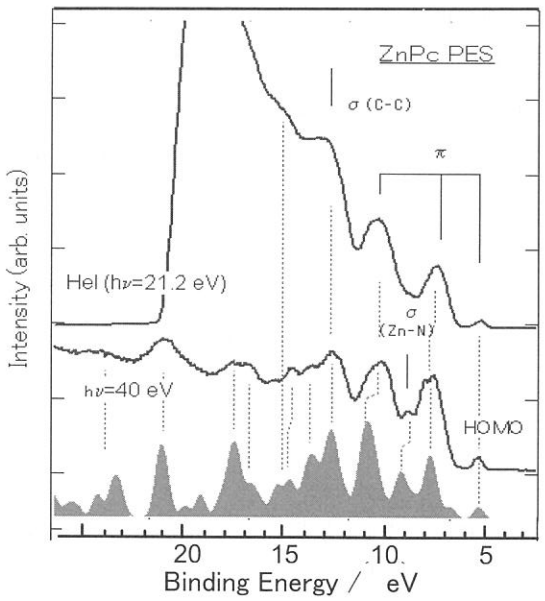

Fig. 1 UPS spectra of ZnPc

In Fig. 2, the corresponding spectra of F_{16}ZnPc at photon energies of 21.2 and 40 eV are.shown. The density of states

by GSCF3 calculations is shown as the shadowed area. In this case, we also see a rather good correspondence between the observed and calculated results, and the spectral features due to the π, σ(C-F), and σ(C-C, C-F) states are assigned as shown in the figure. We note that the levels derived from the lone pair orbitals of the F atoms are concentrated at binding energy around 15 eV.

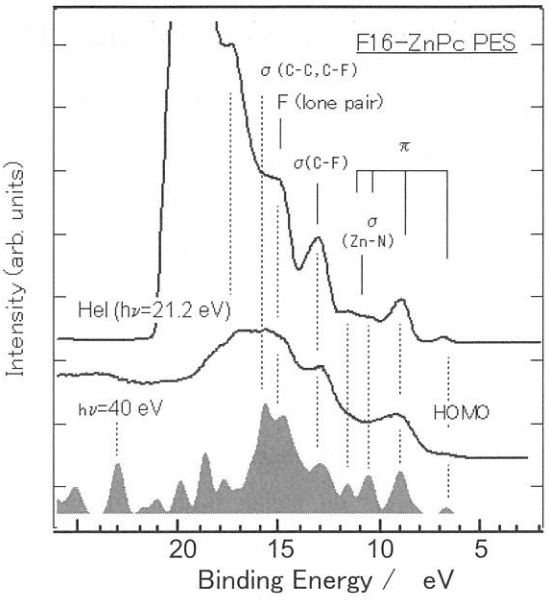

Fig. 2 UPS spectra of F_{16}-ZnPc

When we compare the results for ZnPc and F_{16}–ZnPc, we see that the energy levels are stabilized by fluorination, as expected from the electron-withdrawing nature of the fluorine atoms. In particular, the σ orbitals are more effectively stabilized than the π orbitals. This can be ascribed to the perfluoro-effect, where the σ orbitals are selectively stabilized in planar conjugated systems [3]. Still the π orbitals are also affected, with the HOMO being stabilized by about 1 eV.

It is known that ZnPc shows resonance enhancement of the spectral feature derived from the Zn 3d orbital at binding energy of 15.5 eV with increasing photon energy [4]. In addition, the valley in the He I spectrum becomes shallow in the spectrum at 40 eV. Similar shallowing of the valley is also observed at about 11 eV for F_{16}-ZnPc. These parts may be ascribed to the Zn3d derived Zn-N σ bonds.

Thus we could analyze the valence electronic structures of F_{16}-ZnPc in comparison with that of ZnPc. We are also currently performing NEXAFS studies of these compounds for examining the effect of fluorination to the unoccupied orbitals.

We thank Prof. N. Kosugi of Institute for Molecular Science for providing us the program of GSCF3 calculations.

References

[1] N. Kosugi and H. Kuroda, *Chem. Phys. Lett.*, **74**, 490 (1980)

[2] N. Kosugi, *Theoret. Chim. Acta*, **72,** 149 (1987).

[3] C. R. Brundle M. B. Robin, and N. A. Kuebler, *J. Am. Chem. Soc.*, **94**, 1466 (1972).

[4] E. E. Koch, M. Iwan, K. Hermann, and P. S. Bagus, *Chem. Phys.*, **59**, 249-256 (1981)

(BL8B2)

Electronic Structure of Dialkyl Dichalcogenide Monolayers on Au(111)

T. Miyamae, T. Nakamura, D. Yoshimura†, N. Kobayashi, M. Matsumoto, H. Nozoye

National Institute of Advanced Industrial Science and Technology, Tsukuba, Ibaraki 305-8565, Japan
† Research Center for Materials Science, Nagoya University, Chikusa, Nagoya 464-8602 , Japan

Self-assembled monolayers (SAMs) on metal surfaces present many interesting aspects in resent years from the viewpoints of both basic science and practical applications. Although a variety of substrates and functional groups are known to form SAMs, the thiol/disulfide monolayer on Au has received considerable attention due to its simplicity and ease of preparation. In contrast to the many reports of monolayers derived from organosulfur reagents containing functional groups in the ω-position, there has been relatively little work done to build organic monolayers on metals without using sulfur as the anchor group. The monolayers of heavily chalcogenides such as selenium and tellurium instead of sulfur are promising systems for a variety of applications such as electrical applications, photoresists, photocatalysts, preparation of semiconductor quantum dots of various chalcogenides, etc. due to their importance in technological applications and also due to the possibility of photon-induced electron transfer properties of various selenide and telluride compounds. Moreover, there is little attention for the electronic states which originate from anchored part of adsorbed SAM molecules adsorbed on metal surfaces. In this report, we have studied the molecular conformation and the electronic structural study of alkyl chalcogenides adsorption on Au(111) originated from the difference of the anchored part with ultraviolet photoelectron spectroscopy (UPS).

The Au(111) substrates were prepared by thermally evaporated on mica at a substrate temperature of 693 K. The substrate was immersed into a try toluene diluted dioctyl dichalcogenide solution at a concentration of about 1 mM for 24 h in dry nitrogen atmosphere. After removal from the solution, the samples were rinsed with pure solvent and stored in dried ethanol until measurements under dark condition. ARUPS measurements were carried out at the beamline 8B2 of the UVSOR facility at Institute for Molecular Science. The mu-metal UHV chamber operated at a base pressure in the 2×10^{-8} Pa and consisted of an angle-resolved hemispherical electron energy analyzer of 75 mm mean radius (VG ARUPS-10) mounted with two planes of rotation and a multi channel detector.

Results and Discussion

Figure 1 shows the UPS spectra of C8 disulfide, diselenide, and ditelluride monolayers adsorbed on Au(111) at the incident photon energy $h\nu$ = 40 eV on a binding energy scale relative to the Fermi level. Principally, these spectra resemble each other, indicating analogous electronic structures. Bands A and B are ascribed to pseudo-π and C2s orbital distributed on the alkyl chain, respectively. In Fig, 2, we show the UPS spectra of clean Au(111) and C8 chalcogenides near the Fermi level. In the case of the clean Au(111), the Shockley surface state is clearly observed just below the Fermi level. The quenching of the surface state and the emergence of additional bands attributed to the MOs of the dialkyl dichalcogenide-derived adsorbates. In the case of the C8 disulfide sample, a low intensity feature is observed at approximately 1.5 eV below Fermi level and prior to the Au 5d band onset. We measured with the different photon energies thus changing the

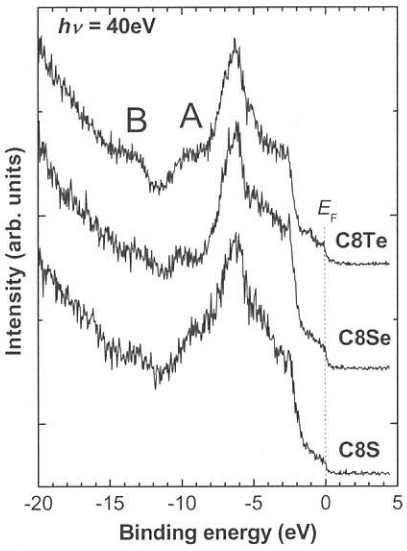

Figure 1 UPS spectra of C8 dichalcogenides adsorbed on Au.

relative cross section between Au 6s and the binding orbital (largely S 2p), and the band has a small contribution of Au 6s. In previous studies of *n*-alkanethiol and dialkyl disulfide on Cu(410) and benzene thiol adsorption of Cu(110), low intensity bands have been observed between 2 and 5 eV [1,2]. Benzenethiol adsorption on Au(111) also shows the low intensity bands at around 1.5 eV, which is considered to the band due to the existence of the Au-S bonding [3]. Similar low intensity bands are also observed at around 1.0 eV for the dialkyl diserenide on Au, and at approximately 1.5 eV for the dialkyl ditelluride on Au. These band observed at around 1.5 eV for dioctyl dicharcogenide adsorbed on Au(111) can thus be taken as evidence of Au-chalcogen bonding.

In our previous report of the conductive-AFM measurements for dioctyl ditelluride-derived monolayer, the dibutyl ditelluride derived adsorbed layer is easily oxidized in air atmosphere than the disulfide and diselenide adsorbed monolayers, and it shows higher resistivity than that of the lighter chalcogenides due to the ease of oxidation reaction in the ambient pressure [4]. By exposing to air for dioctyl ditelluride derived monolayer, this band is completely disappeared, indicating that the Au-Te bonding cleavage proceeds by the oxidation in the atmosphere. The high resisitivity for ditelluride sample is thus caused by the disappearance of the conductive metal-telluride junction due to the cleavage of the Au-Te chemical bond and following the disappearance of the Au-Te bonding state near the Fermi level.

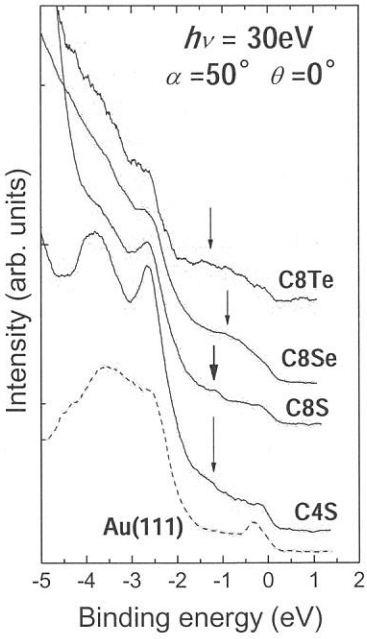

Figure 2 Expanded UPS spectra of C4 and C8 dichalcogenides on Au(111).

References

[1] S. E. Anderson and G. L. Nyberg, *J. Electron Spectrosc. Relat. Phenom.*, **52** (1990) 735.

[2] P. A. Agron, T. A Carlson, W. B. Dress, and G. L. Nyberg, *J. Electron Spectrosc. Relat. Phenom.*, **42** (1987) 313.

[3] C. M. Whelan, C. J. Barnes, C. G. H. Walker, and N. M. D. Brown, *Surf. Sci.*, **425** (1999) 195.

[4] T. Nakamura, S. Yasuda, T. Miyamae, H. Nozoye, N. Kobayashi, H. Kondoh, I. Nakai, T. Ohta, D. Yoshimura, and M. Matsumoto, *J. Am. Chem. Soc.*, **124** (2002) 12642.

(BL8B2)

Intramolecular Energy-Band Dispersion in Oriented Thin Films of Perfluorotetracosane on Cu(100) surface Studied by Angle-Resolved UV Photoemission

D. Yoshimura,[a] T. Miyamae,[b] H. Ishii,[c] S. Hasegawa,[d] K.K. Okudaira,[e,f] N. Ueno,[f] and K. Seki[a]

a) Research Center for Materials Science, Nagoya University, Furo-cho, Chikusa-ku, Nagoya 464-8602, JAPAN

b) Nanotechnology Research Institute, National Institute of Advanced Industrial Science and Technology, 1-1-1 Higashi, Tsukuba 305-8565, JAPAN

c) Research Institute of Electrical Communication, Tohoku University, Aoba-ku, Sendai 980-8577, JAPAN

d) Advanced Research Laboratory, Corporate Research Center, Fuji Xerox Co., Ltd, 1600, Takematsu, Minamiashigara, Kanagawa 250-0111, JAPAN

e) Institute for Molecular Science, Myodaiji-cho, Okazaki 444-8585, JAPAN

f) Department of Materials Science, Faculty of Engineering, Chiba University, Yayoi-cho, Inage-ku, Chiba 263-8522, JAPAN

Poly(tetrafluoroethylene) (PTFE) $(CF_2)_n$ is one of the most prototype polymers, which is the perfluorinated analogue of polyethylene $(CH_2)_n$ with a simple repeating CF_2 unit. PTFE has been widely used for chemical, medical, and high-performance electronic applications due to its excellent chemical and physical properties. Such properties of PTFE are related to its valence electronic structures, and its elucidation is important for the basic science and the practical applications.

The electronic structures of PTFE and its oligomers have been studied both experimentally and theoretically.[1] As an interesting aspect of such one-dimensional polymers, we can expect the formation of intramolecular energy-band along the chain.[2] Many theoretical studies for a PTFE chain have indicated large widths of the bands of the order of 5 eV due to the strong interatomic covalent bond within the chain. Until recently, however, there were no experimental results to be compared with such calculated intramolecular energy-band dispersion relation besides the indirect information of density of states (DOS).

Recently, we have reported the experimental results of the energy-band dispersion for PTFE oligomer observed by ARUPS measurements. In our report, we used the sample, which the long-chain axis is perpendicular to the substrate surface (end-on orientation) and measured the normal-emission spectra with the incident $h\nu$-scanning mode.[3] In this mode, we have to make some assumption about final state of the excited electron. A free-electron-like parabola with a constant inner potential V_0 is often assumed as the final state because the vertical component of wave vector to the surface (along the chain direction) is not conserved.[2] Here, the inner potential is an adjustable parameter of the origin of this parabola. We have evaluated the value of V_0 from the experimental data, but there was some ambiguity for the deduced value.[4]

In the present work, we report on ARUPS studies for the oriented thin films of perfluorotetracosane (n-$CF_3(CF_2)_{22}CF_3$; PFT), an oligomer of PTFE, on Cu(100) surface prepared by in-situ vacuum evaporation. The use of oligomers is based on the theoretical and experimental findings that oligomers more than ten repeating units have very similar electronic structures with infinite polymers. ARUPS measurements with θ-scanning mode with the sample, which the long-chain axis is parallel to the surface enable us to determine the strict energy-band structure of PFT without introducing the inner potential V_0. The parallel component of $\boldsymbol{k}$ to the surface (along the chain direction) is conserved, and we have not to make any assumption about the final state.[5]

ARUPS measurements were carried out at the beamline 8B2 of the UVSOR facility at Institute for Molecular Science. The sample of PFT supplied from Aldrich was used without further purification. Thin films of PFT were prepared by vacuum evaporation at room temperature onto clean Cu(100) substrate. The thickness of PFT was about 0.5 nm as monitored by a quartz oscillator, and the deposition rate was about 0.1 nm/min. In order to minimize the radiation damage, the incident light intensity was reduced less than 60 pA, and the sampling position of specimen was changed after several runs. The absence of the damage effect was confirmed by remeasuring spectra under fixed experimental parameters.

The θ-dependence of the spectra of the PFT/Cu(100) with the incident photon energy of 40eV is shown in Fig. 1. The take-off angle θ was changed in the plane containing the [110] direction of the

substrate. The value of θ is varied from 0° to 70°. In this figure, we found that the topmost band (10.5~13eV in B.E.; band A) and the band derived from C2p atomic orbitals (22~26eV in B.E.; band B) show significant energy shifts due to the intramolecular energy band dispersion. For the detailed peak assignments see Ref. 3. Figures 2(a) and 2(b) are the narrow range scans of the bands A and B, respectively. In Fig. 2(a), the topmost band features of PFT appears at $\theta \geq 45°$, and shows significant energy shift towards lower binding energy side with increasing the take-off angle θ. This band shows the energy minimum at $\theta = 65°$, and at shifts towards higher binding energy side at $\theta = 70°$. In Fig. 2(b), the band derived from C2s atomic orbitals appears at $20° \leq \theta \leq 55°$, and shifts towards lower binding energy side with increasing θ. In Fig. 2(b), we can find non-dispersive peaks at 21.5 and 26eV in B.E. These peaks are attribute to the domain structure that the long-chain axis of PFT is perpendicular to the [110] direction of Cu(100). This exhibits that we have succeeded in preparing the highly oriented film of PFT.[5]

Figure 3 shows the experimentally obtained energy-band structure of PFT plotted in the extended zone scheme. The abscissa is the parallel component of the wave vector $\boldsymbol{k}^{\parallel}$ along the [110] direction of the Cu(100) substrate. In Fig. 3, the binding energy of the topmost band (band A) is the minimum at the Γ point. But the structure of band A is largely different from the one determined in our previous study. This shows that the estimated value of V_0 in our previous study is not reliable one.

We also performed the theoretical simulation of ARUPS spectra based on the independent-atomic-center (IAC) approximation,[5] and the results of the simulation are plotted in Fig.3 with open circles. The observed and simulated data show excellent correspondence. The detailed results of this simulation will be reported soon.

REFERENCES

[1] K. Seki, H. Tanaka, T. Ohta, Y. Aoki, A. Imamura, H. Fujimoto, H. Yamamoto, and H. Inokuchi, *Phys. Scripta* **41**, 167 (1990).

[2] K. Seki, N. Ueno, U. O. Karlsson, R. Engelhardt, and E. E. Koch, *Chem. Phys.* **105**, 247 (1986).

[3] T. Miyamae, S. Hasegawa, D. Yoshimura, H. Ishii, N. Ueno, and K. Seki, *J. Chem. Phys.* **112**, 3333 (2000).

[4] D. Yoshimura, T. Miyamae, H. Ishii, S. Hasegawa, K.K. Okudaira, N. Ueno, and K. Seki, *Surf. Rev. Lett.*, **9(1)** 407 (2002).

[5] D. Yoshimura, H. Ishii, Y. Ouchi, E. Ito, T. Miyamae, S. Hasegawa, K. K. Okudaira, N. Ueno, and K. Seki, *Phys. Rev* B **60**, 9046 (1999)

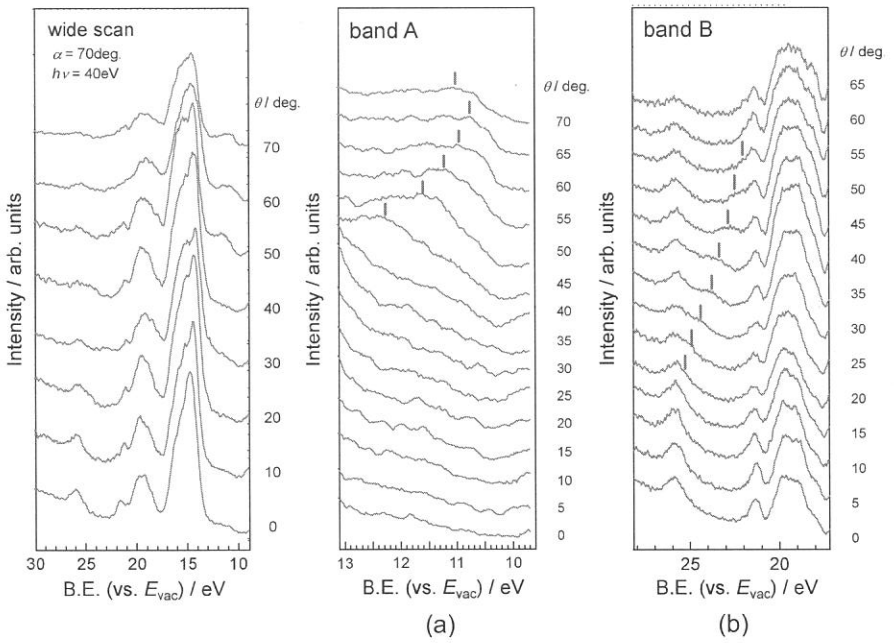

Fig. 1: θ-dependence of ARUPS spectra for PFT/Cu(100).

Fig. 2: Narrow range scans for bands A (a) and B(b).

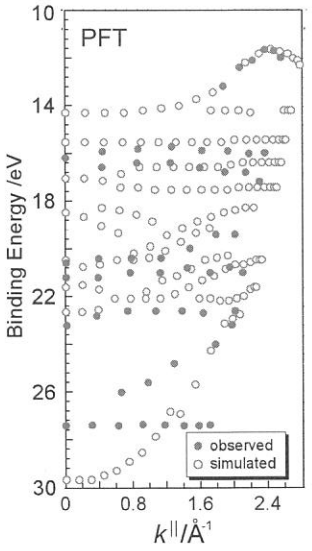

Fig. 3: Band diagram for PFT.